Chapter 6

Magnetically dominated MHD bow shock flows: symmetrical two-dimensional flow around a cylinder

In this Chapter we present numerical simulation results of planar ($v_z \equiv B_z \equiv 0$) field-aligned MHD bow shock flows with top-bottom symmetry around perfectly conducting rigid cylinders.

Fig. 6.1a shows that in the case of hydrodynamic flow ($\vec{B} \equiv 0$) a single shock front is obtained with a concave-inward — towards the cylinder — shape. This topology is also found in experiments of hydrodynamic bow shock flows (Fig. 2.3). As long as the upstream magnetic field strength is small and thermal or dynamic pressure effects dominate, MHD bow shock flows have the same topology as hydrodynamic bow shock flows. An example is shown in Fig. 6.1b. A single-front bow shock with a concave-inward shape is obtained which is entirely of fast 1–2 MHD shock type. It was generally believed until recently that all MHD bow shocks and all bow shocks in space physics plasmas have this topology.

The main result presented in this dissertation is that MHD bow shock flows exhibit an entirely different topology when the upstream magnetic field strength is high and magnetic effects dominate over thermal and dynamic pressure effects such that the intrinsically magnetic phenomena of switch-on shocks and intermediate shocks arise. Because of the peculiar geometrical properties of these types of shocks a complex bow

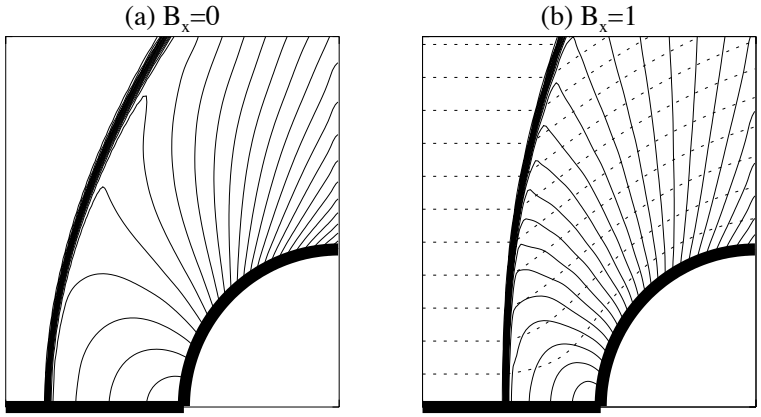

Figure 6.1: *Symmetrical bow shock flows around a cylinder (thick solid) with standard concave-inward topology. The flow comes in from the left. Density contours (thin solid) pile up in the bow shock. Magnetic field lines are dotted. The thick solid horizontal line is a line of symmetry. (a) Hydrodynamic flow:* $B_x = 0$, $M = 3.46$. *(b) Pressure-dominated MHD flow:* $B_x = 1$, $M = 3.46$, $\beta = 0.4$.

shock topology is needed to channel the flow around the obstacle in this magnetically dominated parameter regime. An example of a bow shock flow with this new topology is shown in Fig. 6.2. The new topology involves several consecutive shock fronts of various MHD shock types. It is not really a surprise that several shock transitions occur, because MHD allows for three anisotropic linear wave modes, and the transition from hyperbolic flow far upstream to elliptic flow in front of an obstacle can thus in principle be made through a succession of several shocks of different MHD shock type.

This Chapter is organized as follows. In Sec. 6.1 we explain in terms of the geometrical properties of MHD shocks why the complex bow shock topology of Fig. 6.2 arises when the upstream flow is magnetically dominated and switch-on shocks occur. In Sec. 6.2 we give a detailed interpretation and identification of discontinuities in one example of a complex bow shock flow with the topology of Fig. 6.2. Sec. 6.3 contains a parameter study of symmetrical bow shock flows, which clearly shows that the parameter regime in which the complex bow shock topology arises corresponds to the magnetically dominated regime for which switch-on shocks occur. In Sec. 6.4 we use characteristic analysis to study the complex stationary wave structures present in the magnetically dominated

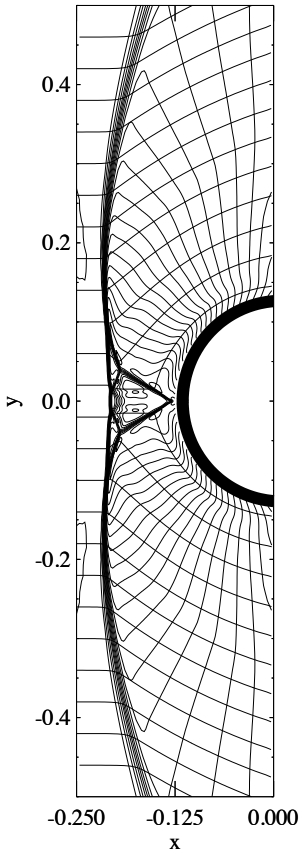

Figure 6.2: *Global view of a magnetically dominated MHD bow shock flow around a cylinder (thick) with upstream parameters* $M_x = 1.5\sqrt{3}$ *and* $\beta = 0.4$. *We show density contours (piling up in the shocks) and magnetic field lines (coming in horizontally on the left). The flow comes in from the left. The leading shock front is slightly dimpled. The upper and lower parts of this front are of the fast type. In the central part of the flow, a second front has separated and is trailing the leading front. Additional discontinuities can be seen in the central interaction region.*

bow shock flows and to identify steady compound shocks. In Sec. 6.5 we discuss the stability of the symmetrical bow shock flow solutions against non-symmetrical perturbations. We conclude briefly in Sec. 6.6.

The results presented in this Chapter have been reported in [150,

149, 151, 152].

6.1 Topology of magnetically dominated bow shock flows

In this Section we discuss the topology of symmetrical field-aligned MHD bow shock flows with magnetically dominated upstream parameters for which switch-on shocks occur. We make extensive use of the properties of MHD shocks which were discussed in Sec. 3.3.2. The discussion is placed in a planar ($v_z \equiv B_z \equiv 0$) 2D context, but most conclusions are equally valid for the 3D case, as is discussed in the next Chapter. Part of our reasoning is similar to the reasoning presented in [147].

6.1.1 The switch-on regime

Switch-on shocks (Fig. 3.8d) can only occur when in the upstream flow

$$B^2 > \gamma p \tag{6.1}$$

and

$$\rho v_x^2 > B^2 > \rho v_x^2 \frac{\gamma - 1}{\gamma(1-\beta)+1}, \tag{6.2}$$

with v_x the velocity along the magnetic field. When the magnetic field strength is small and thermal and dynamical pressure effects dominate, switch-on shocks and intermediate shocks do not occur (e.g. Fig. 3.11). For stronger magnetic fields, however, the intrinsically magnetic phenomena of switch-on shocks and intermediate shocks arise (e.g. Fig. 3.9). Equivalent conditions for the occurrence of switch-on shocks are that the upstream plasma $\beta < 2/\gamma$ and

$$1 < M_{Ax} < \sqrt{\frac{\gamma(1-\beta)+1}{\gamma - 1}}. \tag{6.3}$$

The parameter regime for which magnetic effects dominate and switch-on shocks occur is represented in the $\beta - M_{Ax}$ plane in Fig. 6.3. Because there is a fixed relationship between M_{Ax} and M_x which only involves β and γ, viz. $M_x^2/M_{Ax}^2 = c_{Ax}^2/c^2 = 2\beta/\gamma$, we can also represent the switch-on parameter domain in the $\beta - M_x$ plane, as is done in Fig. 6.3b. Remember from Sec. 3.1.3 that only two non-dimensional numbers are required to parametrize the scales of a given stationary ideal MHD problem, for instance either M_x and β, or M_{Ax} and β.

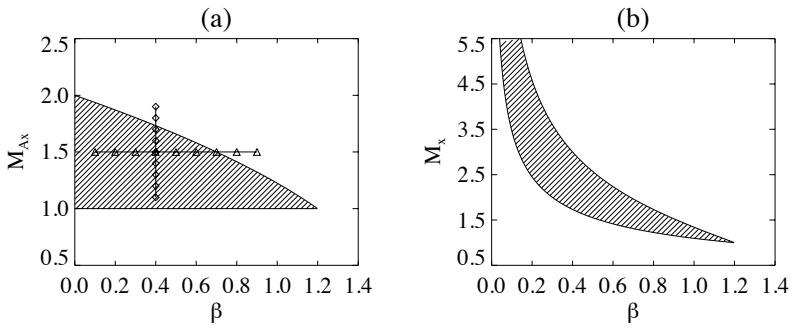

Figure 6.3: *Parameter domain for which states are magnetically dominated and switch-on shocks occur. For $\gamma = 5/3$, switch-on shocks are possible for upstream values of β and M_{Ax} (a) and β and M_x (b) which are located in the shaded regions. In Sec. 6.3, numerically obtained bow shock flows are presented for inflow quantities with fixed $\beta = 0.4$ and M_{Ax} varying from 1.1 to 1.9 (the diamonds on the vertical line in (a)), and with fixed $M_{Ax} = 1.5$ and β varying from 0.1 to 0.9 (the triangles on the horizontal line).*

6.1.2 Shock configurations at perpendicular points

We discuss now what the occurrence of switch-on shocks in magnetically dominated regimes implies for the topology of bow shocks. Two general considerations are important guidelines in our discussion. First, when the upstream flow is magnetically dominated and intermediate shocks can exist, the shock transition from a superfast upstream state of type 1 to a subfast downstream state at the leading front of a bow shock is not necessarily a 1–2 fast shock, but can as well be a 1–3 or a 1–4 intermediate shock. Second, downstream of a leading 1–2 fast shock secondary shocks of slow or intermediate type can in principle be formed, because the downstream state 2 is super-Alfvénic and superslow.

In order to understand the topology of magnetically dominated bow shock flows, it is useful to consider points on shock fronts where the magnetic field is perpendicular to the shock front. We call such points perpendicular points. In Fig. 6.4a we investigate if a shock front which contains a perpendicular point B, can entirely be of the 1–2 fast shock type. When the upstream flow is magnetically dominated (switch-on shocks occur), the 1–2 shock at a perpendicular point has to be a 1–2=3 switch-on shock. Suppose that the switch-on shock at perpendicular point B in Fig. 6.4a deflects the magnetic field upwards. The shock

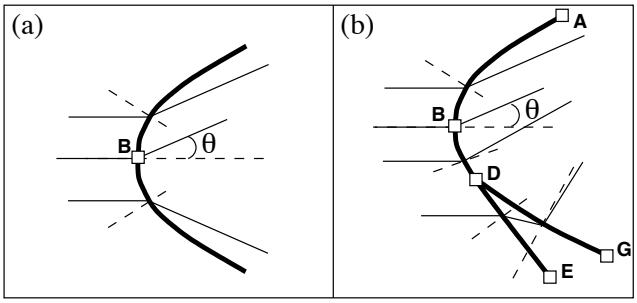

Figure 6.4: *Two proposed topologies for a shock front with a switch-on shock at perpendicular point B for the case of a magnetically dominated upstream flow. Thick lines are shock fronts, thin lines are magnetic field lines, and shock normals are dashed. Point B is a perpendicular point, where the magnetic field is normal to the shock front. The shock at point B is a switch-on shock, which deflects the magnetic field with downstream angle θ. (a) The shock front cannot entirely be of the 1–2 fast type. (b) A complex shock topology is necessary to channel the flow. Shock segment AB is of 1–2 fast type, BD is 1–3 intermediate, DE is 1–2 fast, and DG is 2–4 intermediate, evolving into 2=3–4 switch-off and 3–4 slow along the front.*

segment above point B can entirely be of 1–2 type. Indeed, a fast 1–2 shock deflects the magnetic field away from the normal (Fig. 3.8a), which means upward for this shock segment. If we move downward along this segment towards point B, then the deflection of the magnetic field continuously evolves into a 1–2=3 switch-on shock with upward deflection at point B. The shock segment below point B, however, cannot be of fast 1–2 type, because the magnetic field would be deflected away from the shock normal and thus downward. A 1–2 shock segment can thus not continuously be linked from below to the switch-on shock with upward deflection at point B. The topology of Fig. 6.4a, with a shock entirely of 1–2 type, is thus not possible at a perpendicular point. The question thus arises which shock configurations are possible at a perpendicular point.

Fig. 6.5 shows several allowed shock configurations at a perpendicular point with a superfast upstream state of type 1. In the first row (Fig. 6.5a–d) we show the possibilities for the case that the shock at the perpendicular point is a switch-on shock with upward deflection of the magnetic field. Fig. 6.5a shows that a upper segment of 1–2 fast type can be linked continuously to a lower segment of 1–3 intermediate type in the perpendicular point. Indeed, the 1–2=3 switch-on shock with

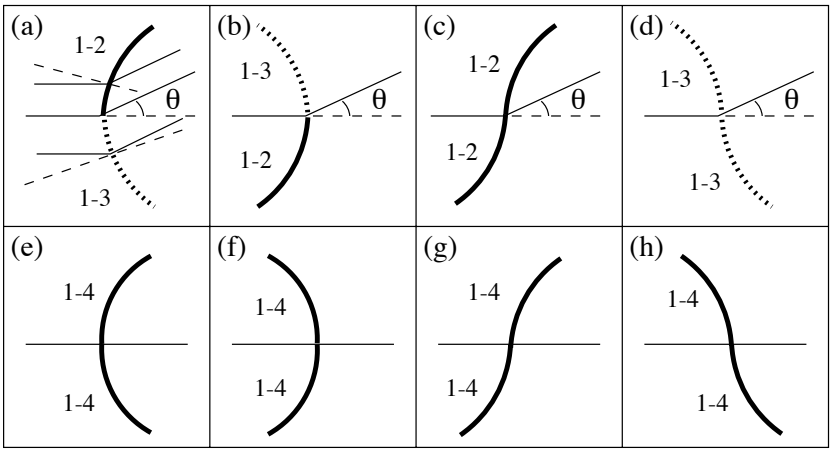

Figure 6.5: *Allowed MHD shock configurations near perpendicular points with magnetically dominated superfast upstream state (switch-on shocks can occur). Magnetic field lines are thin solid, shocks are thick and shock normals are dashed.*

upward deflection is a limit of both the 1–2 fast shock and the 1–3 intermediate shock (see also Fig. 3.9). Fig. 6.5b–d shows other possibilities for the case of a switch-on shock at a perpendicular point.

In the second row of Fig. 6.5 we show the possibilities for the case that the shock at the perpendicular point is a 1–4 hydrodynamic shock (Fig. 3.8f) which does not deflect the magnetic field. The 1–4 hydrodynamic shock is a limit of 1–4 shocks which deflect the magnetic field (see Fig. 3.9), so only 1–4 shock segments can be linked continuously to the 1–4 hydrodynamic shock.

All the configurations of Fig. 6.5 are thus possible near perpendicular points. However, the curved 1–3 and 1–4 intermediate shock segments in Fig. 6.5 can only have a limited extent, because intermediate shocks can only exist for a limited angle between the magnetic field and the shock normal. For the parameter values of Fig. 3.9, for instance, this maximum angle is 16°.

6.1.3 Topology of symmetrical bow shock flows

How can we use the pieces presented in Fig. 6.5 to solve the puzzle of symmetrical bow shock topology in the switch-on regime? Fig. 6.6 proposes two possible topologies for the field-aligned flow around a cylinder. The flow comes in horizontally from the left. The horizontal line through the center of the cylinder is called the stagnation streamline, because the

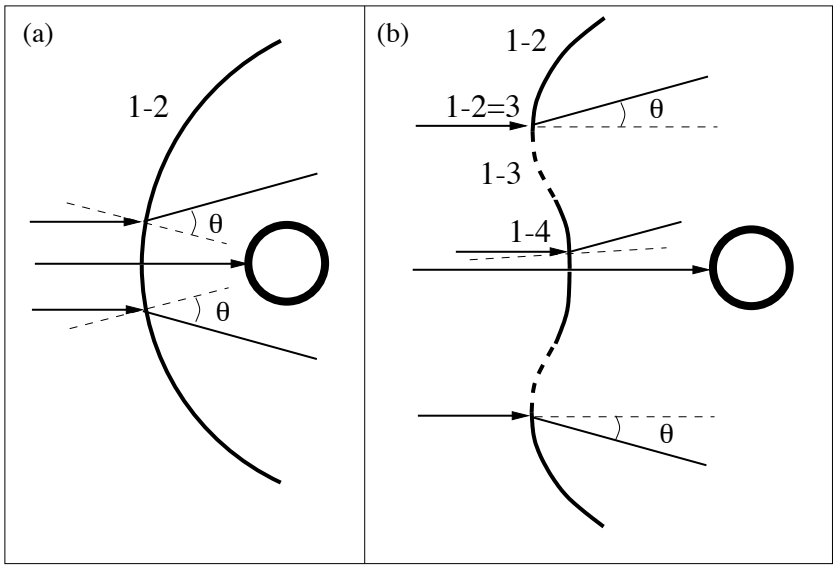

Figure 6.6: *Two proposed symmetrical bow shock topologies for a uniform magnetically dominated flow coming in from the left and obstructed by a conducting cylinder. Magnetic field lines have arrows and shock normals are shown as dashed lines. The horizontal field line terminating on the cylinder is the stagnation streamline. (a) Concave-inward (to the cylinder) shape. The whole shock front (thick line) is of the fast 1–2 type. (b) Dimpled shape proposed by Steinolfson and Hundhausen [147]. Starting from above, the front is first of the fast 1–2 type. At the nose, a 1–2=3 switch-on shock refracts the horizontal incoming magnetic field upward with a finite angle θ. Under the nose the shock front is first of the 1–3 intermediate type, and is then linked to a 1–4 intermediate shock part.*

fluid velocity vanishes on this line at the cylinder. The specification of this flow problem is symmetrical relative to the stagnation streamline. Consequently we expect a flow solution with top-bottom symmetry, and we discuss the topology of such a symmetrical flow here.

On the stagnation line the magnetic field cannot be deflected due to symmetry. This observation immediately rules out the topology of Fig. 6.6a with a single shock front entirely of 1–2 type for magnetically dominated upstream flows. Indeed, a 1–2 shock necessarily has to become a switch-on shock at a perpendicular point, and this is not allowed due to symmetry. This explains why magnetically dominated MHD bow shock flows cannot have the topology of pressure-dominated bow shock flows

(Fig. 6.1) with a single concave-inward shock front of fast 1–2 type! In contrast, for pressure-dominated upstream parameters switch-on shocks do not occur and the angle θ in Fig. 6.6a vanishes at the perpendicular point, such that the bow shock can entirely be of 1–2 fast type.

At the line of symmetry the magnetic field cannot be deflected, so the shock configuration can only be the configuration of either Fig. 6.5e or f. The 1–4 intermediate shock segments can only have a limited extent, however, because for increasing angle between the magnetic field and the shock normal, the 1–4 shock first becomes a 1–3=4 shock and then ceases to exist (Fig. 3.9). Steinolfson and Hundhausen [147] proposed the topology of Fig. 6.6b in the context of their analysis of propagating shocks induced by fast solar Coronal Mass Ejections (CMEs). This topology contains the configuration of Fig. 6.5f near the stagnation line. The configuration of Fig. 6.5a is then linked to the 1–4 shock at the point where the 1–4 shock becomes a 1–3=4 shock (Fig. 3.9). In this configuration the shock front adopts a shape with a *concave-outward dimple* in the central part of the front. The proposed dimple topology contains three perpendicular points, two at the two nose points and one central perpendicular point on the stagnation line. Approaching the top perpendicular point from above, the shock front is first fast 1–2, and becomes 1–2=3 switch-on at the perpendicular point. Going further down, this 1–2=3 shock can continuously evolve into a 1–3 intermediate shock segment. For increasing angle between the magnetic field and the shock normal, the shock type evolves to 1–3=4. Beyond this point the shock becomes 1–4 and concave-outward. At the central perpendicular point the shock becomes a 1–4 hydrodynamic shock.

This proposed solution contains two quite revolutionary ideas: first, the shock front contains a concave-outward part, and second, it is composed of segments of various MHD shock types, which can be linked together in a continuous way. Time-dependent 2D MHD simulations [147, 146] partially confirmed this picture (a dimpled shock front was obtained), and dimpled fronts were also observed in coronagraph images of fast moving CMEs [147, 146, 68].

However, Steinolfson and Hundhausen's time-dependent 2D simulation results for a uniform upstream field did not fully confirm the hypothetical shock geometry of Fig. 6.6b. In their numerical results they found several features for which they could not provide a clear interpretation, including traces of slow shocks, an unusual 'tube' configuration near the symmetry line, and a possible singular point where four shock branches would interact [147].

In our simulation results of stationary bow shock flows with magnetically dominated upstream parameters (Fig. 6.2) we do not find the topology of Fig. 6.6b, although we recover some of its constituting elements. We do find a topology with three perpendicular points. The

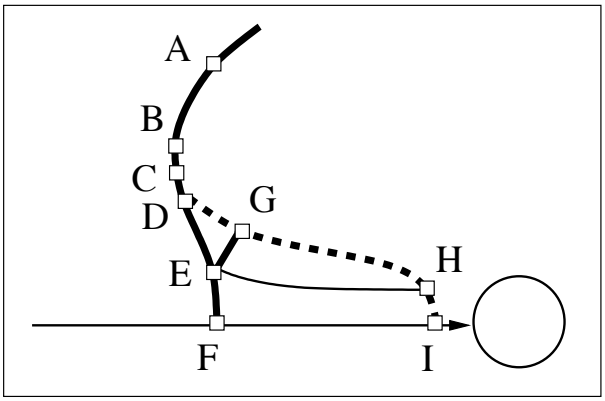

Figure 6.7: *Sketch of the complex multiple-front bow shock topology. In the leading front, shock AB is a 1—2 fast shock, BCD is 1—3 intermediate, DE is 1—2 fast, and EF is 1—4 hydrodynamic. The second front DGHI is 2—4 intermediate (2=3—4 slow switch-off or 3–4 slow at places). EG is a 1=2—3=4 intermediate shock which is sonic both upstream and downstream. EH is a tangential discontinuity, and tangential discontinuities also stretch out from points D, G, and H, along the streamlines towards infinity. At perpendicular point B the shock is a 1–2=3 switch-on shock, at points D and E the shock is of 1–3=4 intermediate type, and at perpendicular point F the shock is 1–4 hydrodynamic. The topology near the perpendicular point B is the topology of Fig. 6.4b.*

topology of the numerically obtained flow pattern (top half) is sketched in Fig. 6.7. Throughout this Chapter we refer to the lettering labels of this Figure for the identification of shock parts. Above the top perpendicular point the shock is indeed of fast 1–2 type, and below this point the shock is of 1–3 type, like in Fig. 6.6b. At the point where the 1–3 shock ceases to exist, however, the shock front splits up into two consecutive shock fronts. This is sketched in Fig. 6.4b. The leading shock segment DE is of the 1–2 fast type, and analysis of the simulation result of Fig. 6.2 learns that the secondary shock segment DG is 2–4 intermediate, evolving into 2=3–4 switch-off and 3–4 slow along the front. The combination of the fast and the intermediate shock can deflect the magnetic field such that field lines merge continuously downstream of the so-called λ-point D where the three shock segments meet.

Near the stagnation line in Fig. 6.2 we find the configuration of Fig. 6.5e. At the point where the 1–4 shock ceases to exist, it splits up into a fast 1–2 shock followed by a 1=2–3=4 intermediate shock. This cannot

be seen very clearly in Fig. 6.2, but shock segments are clearly identified in the next Section. In general it seems that the leading shock front splits into two consecutive fronts at 1–3=4 points beyond which intermediate shocks can no longer exist.

In this Chapter we present simulations of the 2D steady state MHD bow shock problem with magnetically dominated upstream flow (switch-on shocks occur). In contrast to the time-dependent flows considered by Steinolfson and Hundhausen [147], our bow shock solutions are stationary in time, which allows for higher grid resolution and greatly facilitates a clear interpretation. The topology we obtain in our simulation results contains some elements of the topology proposed in Fig. 6.6b, but the resulting bow shock flow is quite more complicated than could be anticipated from the important earlier work of Steinolfson and Hundhausen [147]. The leading shock front is followed by a second shock front, and other discontinuities can be identified between the two fronts. Our solution reveals and explains much richer and more complex physics not anticipated in the work of Steinolfson and Hundhausen [147]. Clearly an additional level of complexity is present: not only do shocks of several different types form in the leading front, but multiple shock fronts are necessary to channel the magnetically dominated flow around the obstacle. It is conceivable that our results on shock topology in stationary magnetically dominated flows can also be important for shock propagation in time-dependent flows in this parameter regime.

6.2 Detailed interpretation and identification of discontinuities in a magnetically dominated bow shock flow

In this Section we analyze in detail the flow of a planar ($v_z \equiv B_z \equiv 0$) superfast MHD fluid around a perfectly conducting rigid cylinder for magnetically dominated upstream parameters (switch-on shocks occur). The angle between the magnetic field and the velocity field cannot be varied because the flow is necessarily field-aligned, so the problem of stationary 2D MHD flow around a perfectly conducting cylinder has only two free parameters which parametrize the scales, for instance β and M_A or β and M. The analogous hydrodynamic problem has only one free parameter, for instance M.

For the incoming flow we choose $\beta = 0.4$, which implies a critical Alfvénic Mach number $M_{Ax,crit} = 1.732$ (Eq. 6.3). We choose the Alfvénic Mach number of the incoming flow $M_{Ax} = 1.5$, such that the upstream flow is magnetically dominated and allows for switch-on shocks (see also Fig. 6.3a). The x axis being horizontal, we can choose $\rho = 1$

and $B_x = 1$ (implying that the Alfvén speed $c_{Ax} = 1$). The pressure and velocity can then be determined from β and M_{Ax}, yielding $p = 0.2$ and $v_x = 1.5$ (such that the acoustic Mach number $M_x = 1.5\sqrt{3}$). Finally, we take $B_y = 0$ and $v_y = 0$. As the resulting stationary ideal MHD flow is scale invariant, we can freely choose the radius of the cylinder. We take $r = 0.125$ and the cylinder is placed at the origin of the coordinate system.

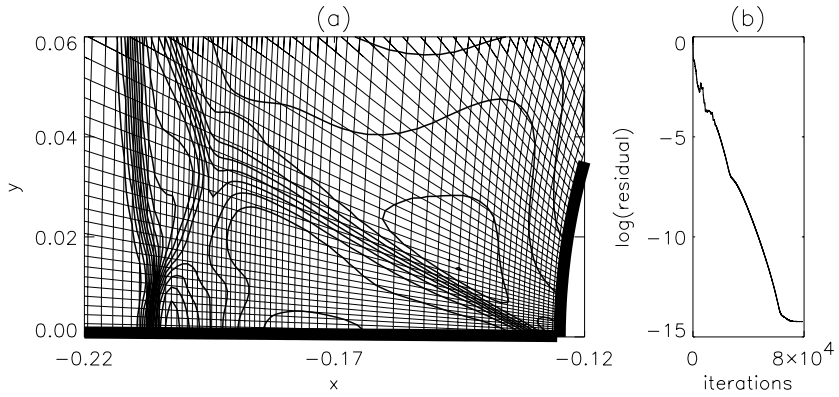

Figure 6.8: *(a) Detail of the simulation grid (80 × 80) with density contours. The thick solid lines represent simulation domain boundaries with ideal wall symmetry. (b) Convergence of the simulation to a steady state. The logarithm of the root mean square of the density residual is shown as a function of the number of iterations.*

The numerically computed stationary solution of Fig. 6.2 is obtained through time relaxation starting from a uniform initial condition, which is taken to be the above described uniform inflow. We look for a stationary solution, and the steady flow necessarily has to be field-aligned. The complete setup of this problem — initial condition, boundary conditions and the MHD equations — satisfies top-bottom symmetry relative to the stagnation line. We thus expect a stationary solution which satisfies this top-bottom symmetry as well. In our numerical simulations we explicitly impose this symmetry by performing the calculations only in the upper left quadrant bounded from below by the stagnation streamline, and by specifying symmetry boundary conditions on this lower boundary. These boundary conditions are the same as for a perfectly conducting wall. The simulated bow shock flow in the upper quadrant can thus also be thought of as a 2D model flow over a perfectly conducting plate (the stagnation line) with a semi-circular bump or corner. In the case

of the full flow around the cylinder, the question of the stability of the symmetrical solution against non-symmetrical perturbations turns out to be important, as is discussed in Sec. 6.5.

We simulate the flow in the upper left quadrant, on a 120×120 stretched elliptic polar-like structured grid, extending to $x = -0.35$ on the x axis, and to $y = 1.4$ on the y axis. Part of the simulation grid is shown in Fig. 6.8a. The grid resolution is increased near interesting features of the flow by accumulating or clustering grid points. This grid accumulation is done in a dimension by dimension way. In the i direction, the grid is clustered near the perpendicular point on the leading shock front, and near the stagnation point. In the j direction, the grid is clustered near the stagnation line. We use ghost cells to specify the boundary conditions (Sec. 4.2.6). On the left, we impose the uniform superfast incoming flow. The cylinder wall is an ideally conducting rigid wall. The lower border of the simulation domain satisfies ideal wall symmetry as mentioned above. The right outflow condition is superfast, so there we extrapolate all quantities to the ghost cells. The flow evolves in time until a converged steady state bow shock solution is obtained, and Fig. 6.8b shows the convergence of the density residual.

For our present simulations, we use the second order scheme with Lax–Friedrichs numerical flux function (Sec. 4.2.5). In Chap. 9 we report on our experience with other numerical flux functions for this bow shock problem. We use Powell's source term technique to keep the $\nabla \cdot \vec{B} = 0$ constraint satisfied (Sec. 4.4), and in Chap. 9 we show that a projection scheme leads to essentially the same results.

We now show how the types of all MHD discontinuities arising in the flow of Fig. 6.2 can be clearly determined.

In Fig. 6.9 we show a detailed section of the computed flow in the half plane above the stagnation streamline. D–E is a fast shock with $B_{y,1}$ almost vanishing upstream, so it is almost a fast switch-on shock. E–F is a 1–4 intermediate shock. It is probably slightly concave-inward at locations on the front away from point F, like in Fig. 6.5e, and thus unlike the concave-outward 1–4 central part in Steinolfson and Hundhausen's proposed solution (Fig. 6.6b). At the resolution of our simulations, however, no definite conclusions can be made about this orientation.

At point F, the shock is definitely of the hydrodynamic 1–4 type. E–G is an intermediate shock, because it clearly contains the dashed $M_A = 1$ contour (showing that the flow goes from super-Alfvénic to sub-Alfvénic upon passing through the shock), and because the field lines are flipped over the normal. Bear in mind that the Alfvénic Mach number M_A does not depend on the direction for the case of field-aligned flow. Below it is shown that shock E–G is a 1=2–3=4 intermediate shock.

D–G–H–I is an intermediate shock with an upstream Alfvénic Mach number (slightly) greater than one, and with magnetic field lines that

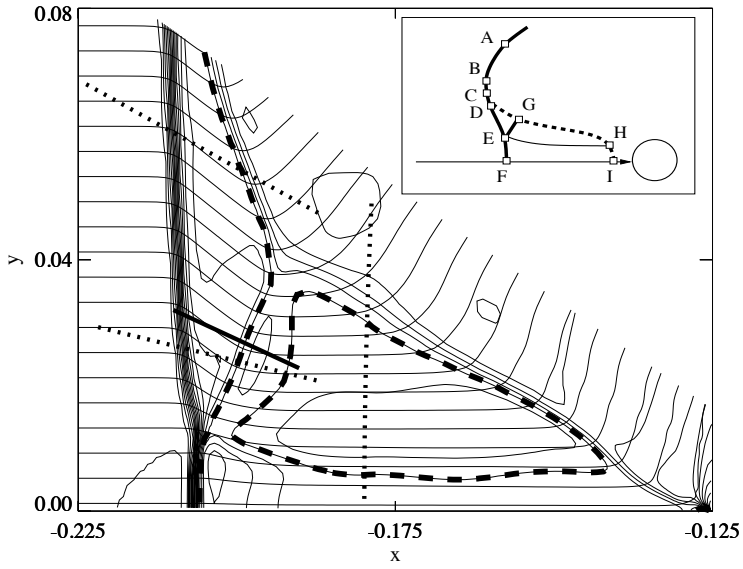

Figure 6.9: *Detail of the solution in the half plane above the stagnation streamline. We show Alfvénic Mach number contours (piling up in the shocks) and magnetic field lines (coming in horizontally on the left). The dashed line is a contour where the Alfvénic Mach number exactly equals one. This information together with the refraction of the field lines serves to identify the shocks as fast, hydrodynamic, and intermediate (see the text).*

are flipped over the normal. At various places along the shock front, the upstream intermediate Mach number approaches one and the downstream magnetic field becomes normal to the front, meaning that the shock becomes 2=3–4 slow switch-off and even 3–4 slow at places.

E–H is a tangential discontinuity. Other tangential discontinuities are stretching out from points D, G, and H along the streamlines to infinity.

E–F is very reminiscent of a Mach stem as it occurs in Hydrodynamic shock reflection [169]. A priori the point E could lie on the stagnation streamline, in which case this point would be a singular point on this streamline where four shock branches interact. In such a situation, the stagnation streamline would not be a shock normal. In such a hypo-

thetical singular point, the $\nabla \cdot \vec{B} = 0$ constraint could be satisfied if the jump in B_y in the y direction is exactly the same (with opposite sign) as the jump in B_x in the x direction. A solution with such a singular point is found for simulation on a grid with low spatial resolution. With sufficient resolution however, the shock part E-F appears, reducing the singularity to three branches interacting in point E. An interaction point where four branches meet, seems thus to be avoided. This may be a more general feature of MHD shock interaction.

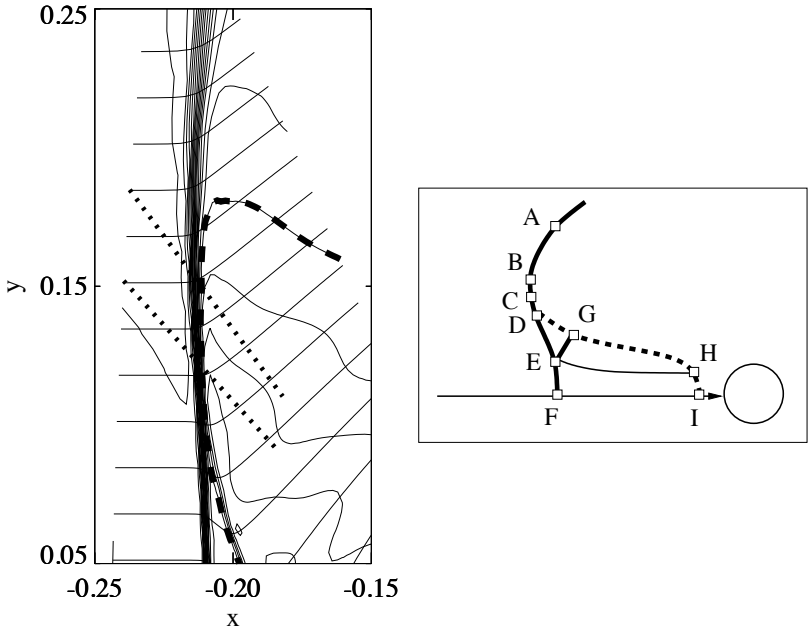

Figure 6.10: *Detail of the solution close to the 'nose'. We show Alfvénic Mach number contours and magnetic field lines. The dashed line is a contour where the Alfvénic Mach number exactly equals one. This information together with the refraction of the field lines serves to identify the shocks as fast and intermediate (see the text).*

In Fig. 6.10 we show a detail of the region close to the 'nose' point B. The refraction of the field lines (away from the shock normal) above point B shows that this part of the shock is a fast shock. The shock at point B is a 1–2=3 fast switch-on shock, because the tangential field component is switched on, and because the downstream Alfvénic Mach number equals one. B–C–D is an intermediate shock, because it clearly

contains the dashed $M_A = 1$ contour, and because the field lines are flipped over the normal. Shock B–C–D is of the 1–3 type, which can be merged continuously with the fast 1–2=3 switch-on shock in point B.

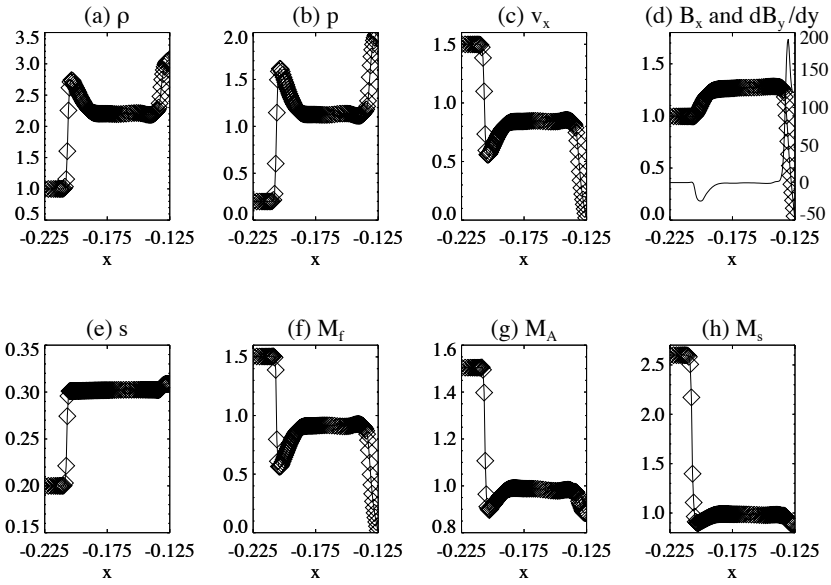

Figure 6.11: *Plots of the variables along the stagnation streamline. From left to right, the uniform incoming flow first jumps in the hydrodynamic shock, followed by a slow rarefaction, which brings the flow back to uniform. Close to the cylinder we pass the intermediate shock. The flow is then brought to the stagnation point in a continuous diverging compression. The variation of $\partial B_y/\partial y$ in (d) (thin line, axis on the right) shows that the flow is effectively 2D at various locations on the stagnation line.*

In Fig. 6.11 we show plots of the variables along the stagnation streamline. The simulation results presented in this plot were obtained using a projection method, because the Powell approach computes slightly inaccurate values near the stagnation point (see Chap. 9). The first feature we encounter when we go from left to right, is a discontinuity which corresponds to the hydrodynamic shock at point F. The RH relations for the shock on the stagnation streamline are simple and can be solved easily [114], resulting in downstream quantities $p = 1.64$, $\rho = 2.77$, $v_x = 0.542$, and $s = 0.300$. The jumps of the density, pressure, velocity, and entropy in Fig. 6.11 agree well with the jumps calculated from the

RH relations. The fast, Alfvénic and slow Mach number all jump from above one to under one, indicating a 1–4 intermediate shock. The magnetic field does not show a jump, consistent with a purely hydrodynamic shock.

Going further to the right, we see that we pass through a rarefaction to reach a constant state. This slow rarefaction converges the flow slightly towards the stagnation streamline. Although the flow near the stagnation line may appear to be close to a 1D flow in Fig. 6.9, the flow is in fact 2D at various places along the stagnation line. In Fig. 6.11d we plot $\partial B_y/\partial y$ (thin line), indicating that the flow is 2D in this rarefaction region. The density decreases in the main direction of the converging flow on the stagnation line, because the velocity (v_x) is increasing and $\nabla \cdot (\rho \vec{v}) = 0$. B_x is not significantly influenced by the increasing v_x because the field is aligned to the flow. However, B_x increases along the flow because of the 2D effect of converging flow in the y direction perpendicular to the stagnation line. This flow component causes the field lines to converge towards the stagnation line, as can be seen in Fig. 6.11d: $\partial B_x/\partial x$ balances $\partial B_y/\partial y$ such that $\nabla \cdot \vec{B} = 0$.

Going further to the right, we pass a region where the flow is uniform. The flow becomes 2D again as we approach the stagnation point at the cylinder, as can be seen in Fig. 6.11d. This is no surprise, because in general every stationary stagnation point flow is necessarily 2D due to the requirement of mass conservation ($\nabla \cdot (\rho \vec{v}) = 0$). Indeed, a stagnation point can clearly not be reached by means of a stationary 1D flow (neither a shock nor a continuous flow), because a 1D flow can not bring ρv_x down from a finite value to a value of zero at the stagnation point.

As an illustrative example of a stationary 2D stagnation point flow, we show in Fig. 6.12 how a stagnation point is reached in a traditional pressure-dominated single-front MHD bow shock flow, which is obtained by choosing the inflow velocity outside of the switch-on region (Eq. 6.3): $\rho = 1$, $p = 0.2$, $v_x = 2$, $v_y = 0$, $B_x = 1$, and $B_y = 0$ at the inflow, resulting in inflow Mach numbers $M_{Ax} = 2$ and $M_x = 2\sqrt{3}$ ($\beta = 0.4$). The stagnation point is reached in a continuous (constant-entropy) 2D compressive diverging flow region behind the shock front.

In our simulation, the 2D stagnation point flow is complicated by the presence of intermediate shock D–G–H–I. Fig. 6.2 shows that point I lies very close to the cylinder. In this small region between point I and the cylinder we expect the 2D stagnation point flow. Because this region is extremely small compared to the dimensions of the other features in our simulation, we could not avoid a comparatively low numerical resolution in this region. Moreover, the curvature of the intermediate shock front at point I is very large and may even be singular, which makes the post-shock flow 2D and complicates the interpretation of the shock as a 1D shock.

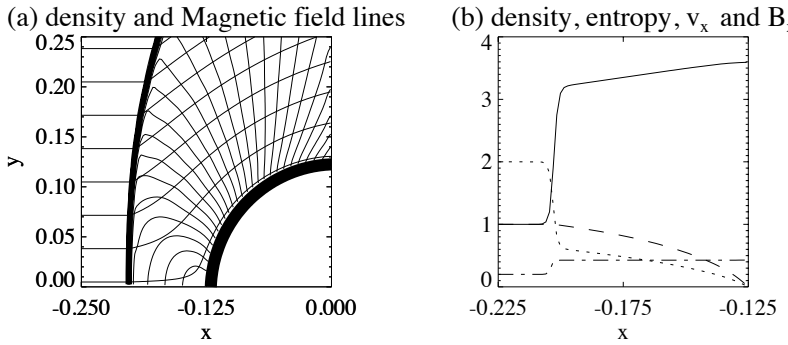

Figure 6.12: *Simulation of a pressure-dominated MHD flow with a single-front bow shock (inflow Mach numbers $M_{Ax} = 2$ and $M_x = 2\sqrt{3}$, and $\beta = 0.4$). (a) Flow near the cylinder. (b) Stagnation line variables. Behind the shock, the flow variables are brought to their stagnation point values in a continuous compressive diverging flow. B_x is dashed, v_x dotted, s dash–dotted, and ρ full.*

All these complications make the interpretation of the simulation results near the cylinder quite difficult. However, we can propose the following possible interpretation for the variation of the flow variables near the cylinder in Fig. 6.11.

The location of the small jump in entropy in Fig. 6.11e close to the cylinder can reasonably be identified with the point I of Fig. 6.9, where the intermediate shock D–G–H–I intersects the stagnation line. This entropy jump is located at a finite distance from the cylinder, which means that there is a small but finite standoff distance between the shock and the cylinder. In the small constant-entropy region between point I and the cylinder, we can expect a continuous 2D stagnation point flow analogous to the flow in Fig. 6.12. The variation of ρ, v_x, and B_x close to the cylinder in Fig. 6.11 appears to be consistent with the continuous variation of these quantities in the stagnation point flow of Fig. 6.12.

Although not conclusively proven, this interpretation of the flow near the cylinder in Fig. 6.11 as a weak shock followed by a 2D compressive diverging stagnation point flow is physically reasonable since it is consistent with the simulation data and since it establishes a clear analogy with less complicated stagnation point flows. It will be interesting to see if future simulations with more powerful numerical techniques will confirm all the details of this interpretation of the highly complicated stagnation point flow.

In Fig. 6.13 we show plots of some variables along several instruc-

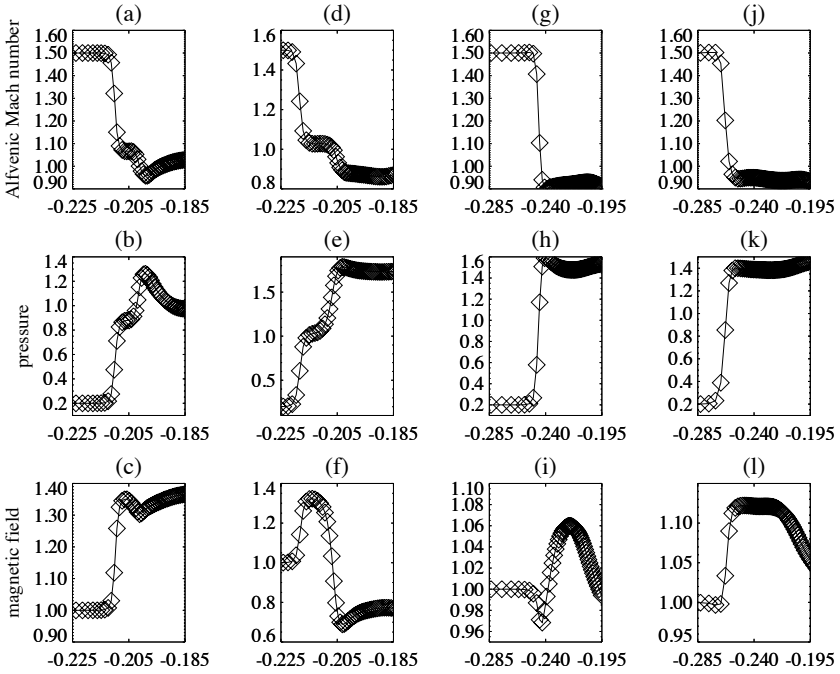

Figure 6.13: *Alfvénic Mach number (a,d,g,j), pressure (b,e,h,k), and magnetic field (c,f,i,l) along various cuts through the simulation domain. (a-c) Cut along the lower dotted line cutting the leading front in Fig. 6.9. (The lower axis shows the distance to the center of the cylinder.) We pass the fast shock, and then the intermediate shock followed by a rarefaction. (d-f) Cut along the upper dotted line cutting the leading front in Fig. 6.9. We pass the fast shock, and then the intermediate shock. (g-i) Cut along the lower dotted line cutting the leading front in Fig. 6.10. We cross the intermediate shock. (j-l) Cut along the upper dotted line cutting the leading front in Fig. 6.10. We cross the intermediate shock.*

tive 1D cuts. Figs. 6.13a-c show a cut along the lower dotted line cutting the leading front in Fig. 6.9 under an angle of $\theta = 13.82$ degrees. First we cross the fast shock. Then the intermediate shock brings the Alfvénic Mach number from above one to under one. Figs. 6.13d-f show a cut along the upper dotted line cutting the leading front in Fig. 6.9 ($\theta = 29.25$). Again we cross the fast shock first. Then we cross the intermediate shock, with the upstream Alfvénic Mach number close to one. Figs. 6.13g-i show a cut along the lower dotted line cutting the leading front in Fig. 6.10 ($\theta = 47.66$). We cross only one shock, which

is of the intermediate type, because it brings the Alfvénic Mach number from above one to under one. Figs. 6.13j-l show a cut along the upper dotted line cutting the leading front in Fig. 6.10 ($\theta = 53.40$). We cross the same intermediate shock.

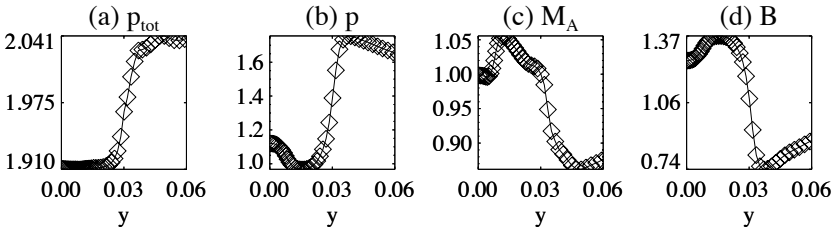

Figure 6.14: *Cut along the vertical dotted line in Fig. 6.9. We first cross the tangential discontinuity, with a jump in pressure but not in total pressure. Then we pass the intermediate shock.*

In Fig. 6.14 we show plots of some variables along the vertical dotted line in Fig. 6.9. Where the pressure jumps for the first time, we pass through the tangential discontinuity (a little more smeared out than the shocks), as is proved by the continuity of the total pressure here. The next jump is the intermediate shock, with an upstream Alfvénic Mach number close to one. (This profile is a little smeared out because we cross it at a large angle).

It is interesting to look for the presence of 1=2–3 and 2–3=4 sonic intermediate shocks in our 2D simulation results, as they are a manifestation of the non-convex nature of the MHD equations, as was explained in Sec. 3.3.5. Bear in mind that we call a shock 'sonic' whenever the normal plasma speed equals any of the MHD wave speeds on the upstream or the downstream side. We look for shocks with a conspicuous rarefaction attached, as seen in compound shocks of the time-dependent non-convex MHD system, and investigate if the shock is sonic where the rarefaction is attached.

Let us first consider the 1–4 hydrodynamic intermediate shock on the stagnation streamline. It is followed by a slow rarefaction (Fig. 6.11), but Fig. 6.11f-h shows clearly that the flow is not sonic where the rarefaction is attached to the shock. This shock is thus not of the sonic type, and in this example the rarefaction is a 2D effect, as noted before. It serves to bring the Alfvénic Mach number from its downstream value lower than one to a value close to one, necessary for the shock at point I.

Intermediate shock C–D (Fig. 6.13h-i) is followed by a rarefaction, in contrast to intermediate shock B–C (Fig. 6.13k-l; the different behavior

of the post-shock magnetic field is striking). Shock D–G–H–I seems to be followed by a rarefaction as well (Figs. 6.13e-f, 6.14d). For all of these structures, the flow is, however, not sonic where the rarefaction is attached to the shock.

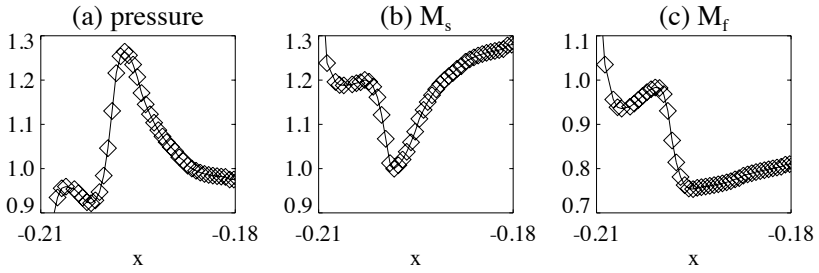

Figure 6.15: *Cut along the solid line normal to the intermediate shock E–G in Fig. 6.9. The intermediate shock is preceded and followed by rarefaction regions. The normal fast Mach number equals one where the upstream (left) rarefaction is attached to the shock. The normal slow Mach number equals one where the downstream rarefaction is attached to the shock. The intermediate shock is thus a 1=2–3=4 shock.*

Finally intermediate shock E–G remains to be investigated. This shock is followed by a distinct rarefaction and preceded by another (weak) rarefaction (Fig. 6.13b-c and Fig. 6.15a). A detailed analysis of the speeds along the solid line normal to shock E–G in Fig. 6.9 shows that the intermediate shock is a 1=2–3=4 shock, as the downstream normal slow Mach number and the upstream normal fast Mach number are both equal to one (Fig. 6.15b-c). The flow is thus sonic on both sides of the shock. This is a clear manifestation of the non-convexity of the MHD equations in a steady state 2D flow.

It has been shown recently by Myong and Roe [109, 110] that this type of 1=2–3=4 shock can be present in the analytical solution of planar xt Riemann problems, embedded in a double xt compound wave. The stationary 2D rarefaction–shock–rarefaction structure of our xy simulation result could be more closely related to this double xt compound wave, if the steady state rarefactions preceding and following the sonic shock are simple waves, and not merely 2D effects similar to the rarefaction following the hydrodynamic shock on the stagnation line. To investigate this, it is interesting to compare the characteristic structure of this 2D stationary structure in the xy plane to the characteristic structure of the double compound wave in the xt plane, which has simple wave rarefactions. This is investigated in Sec. 6.4 using the character-

istic properties of the steady state MHD equations. There it is shown that shock E–G is a genuine stationary double compound shock, mathematically completely analogous to the time-dependent double compound shock analyzed by Myong and Roe.

6.3 Parameter study of symmetrical bow shock flows

In this Section we report on a detailed parameter study of symmetrical field-aligned bow shock flows around a cylinder. We study how the shape and topology of the bow shock solution which was presented in the previous Section for one particular set of parameter values in the switch-on domain, changes when parameters are varied within the switch-on domain and when parameters are taken outside the switch-on domain. We present numerical simulation results for the values of the parameters β and M_{Ax} which are indicated by the triangles and diamonds in Fig. 6.3a.

Fig. 6.16 shows global views of the bow shock solutions for a fixed $\beta = 0.4$ with M_{Ax} varying from 1.1 to 1.9. We take $c_{Ax} = 1$ in the inflow, such that $M_{Ax} = v_x$. It follows from Eq. 6.3 that the critical Alfvénic Mach number under which switch-on shocks can exist is $M_{Ax} = 1.732$. For inflow speeds much faster than the Alfvén speed ($c_{Ax} = 1$), the upstream flow is pressure-dominated (no switch-on shocks). For pressure-dominated upstream parameters the bow shock has the traditional single-front topology that is also encountered in hydrodynamic bow shocks. When the inflow speed drops below 1.732, however, the flow becomes magnetically dominated (switch-on shocks occur). A concave-outward dimple forms in the leading shock front and a second shock front appears. This change in shape and topology of the bow shock flow thus happens exactly when the inflow speed becomes lower than the critical speed under which switch-on shocks are possible.

Fig. 6.17 shows a detailed representation of the flow near the stagnation streamline for the bow shock solutions with varying inflow speed of Fig. 6.16. For inflow velocities below the critical switch-on value for the inflow speed ($M_{Ax} < 1.732$), the leading shock front has a dimpled shape. The dimpling becomes much more pronounced as the inflow velocity decreases. Below the critical inflow speed, a second shock front appears which trails the leading shock front, and additional discontinuities are present between the two shock fronts. All the shocks and discontinuities present in the topology sketch of Fig. 6.7 seem to be present in all the flows. Inspection of the way in which the field lines are refracted when they pass the shocks, reveals that the shocks in all the flows are of the same type as the shocks in the model flow of Fig. 6.2 which was discussed in detail in Sec. 6.2, and this conclusion is confirmed

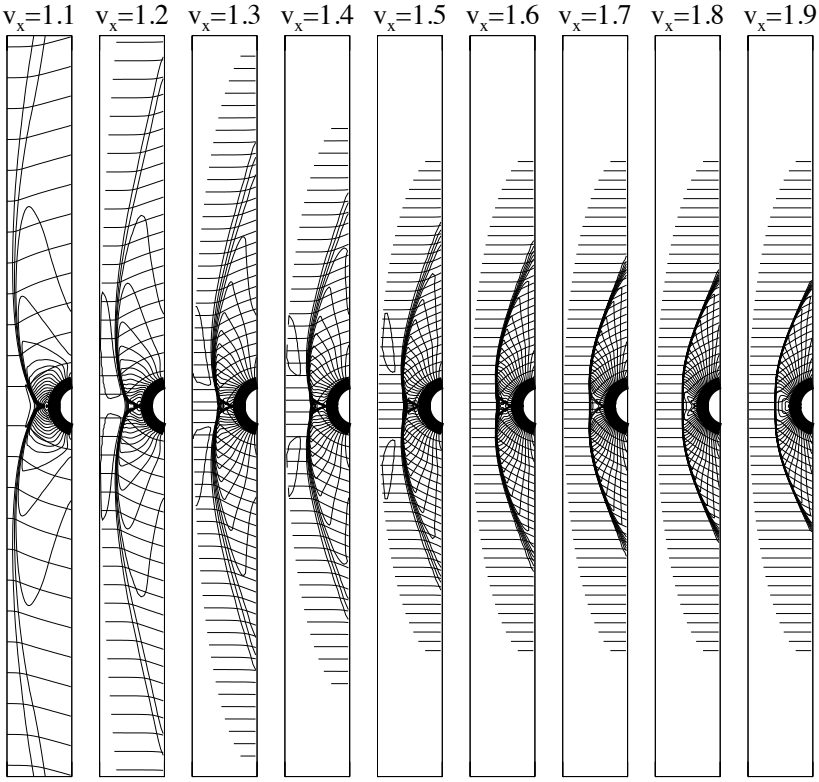

Figure 6.16: *Stationary bow shock solutions for fixed* $\beta = 0.4$ *and for varying inflow speeds (*80×80 *grids,* $x \in [-0.35, 0]$, $y \in [-2, 2]$*). Density contours pile up in shocks, and streamlines come in horizontally from the left. For inflow speeds much faster than the Alfvén speed (*$c_{Ax} = 1$*), the upstream plasma is pressure-dominated (no switch-on shocks), and the bow shock has the traditional single-front topology that is also encountered in hydrodynamic bow shocks. When the inflow speed drops below* 1.732 *however, the inflow becomes magnetically dominated, which means that switch-on shocks occur. For these magnetically dominated inflows a concave-outward dimple forms in the leading shock front and a second shock front appears.*

by detailed analysis of upstream and downstream Mach numbers, along the lines of the detailed analysis in the previous Section. For smaller inflow velocities, the central interaction region becomes smaller and the leading shocks become weaker while the trailing shock becomes stronger.

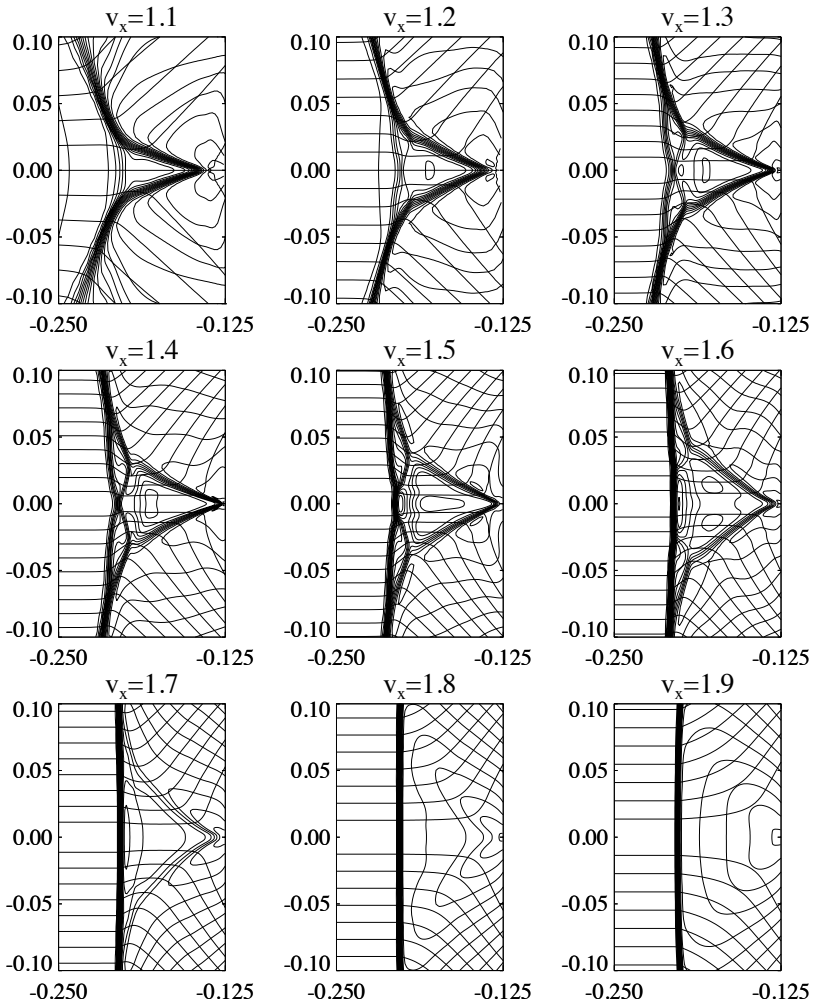

Figure 6.17: *Detailed representation of the flow near the stagnation streamline for the bow shock solutions with varying inflow speed and fixed $\beta = 0.4$ (80×80 grids). Density contours pile up in shocks, and streamlines come in horizontally from the left. When the upstream flow is magnetically dominated, the leading shock front dimples and a second shock front appears. Additional discontinuities can be seen between the two shock fronts.*

As a consequence, the shock E–G of Fig. 6.7 can not be identified for the flow with $v_x = 1.1$ with the resolution of Fig. 6.17. More detailed

simulations and plots (not shown) do, however, show that shock E–G is present also for the flow with $v_x = 1.1$. For inflow velocity $v_x = 1.7$, close to the critical velocity of $v_x = 1.732$, the secondary shock fronts become weak and shock E–G can hardly be identified with the resolution of Fig. 6.17. For $v_x = 1.8$ the secondary (stationary) waves are still present, but they have not steepened into shocks any more. The secondary waves have disappeared almost completely for $v_x = 1.9$, and the simple single-front bow shock topology of Fig. 6.6a is recovered. We can thus conclude that for all the flows with magnetically dominated upstream parameters ($1 < M_{Ax} < 1.732$), the topology of Fig. 6.7 is a universal feature. The shapes, sizes and shock strengths of the shock parts present in the topology of Fig. 6.7, vary when M_{Ax} is varied within the switch-on region.

The dimple effect is more pronounced for smaller inflow Alfvénic Mach number M_{Ax}. This can be explained by the fact that when for magnetically dominated upstream flows v_x is increased towards v_{crit}, the maximum angle between the upstream magnetic field and the shock normal for which intermediate shocks can occur decreases. This means that for faster upstream flows, point D in Fig. 6.7, where the shock is of 1–3=4 type and beyond which the shock front splits up, lies closer to the perpendicular nose point B. The 1–3 intermediate shock segment which forms part of the dimple, is thus shorter and less deep for higher v_x. For instance, Figs. 3.9 and 3.10 show that for $v_x = 1.2$ the angle between the horizontal and the 1–3 shock front at point D is approximately 16°, whereas for $v_x = 1.5$ this angle is only 3°. This expected behavior is indeed observed in Figs. 6.16 and 6.17.

Above we discussed how the flow manages to go around the obstructing cylinder by adjusting the bow shock shape and topology to the inflow Alfvénic Mach number. Hereby the plasma β value was fixed to 0.4. Below we fix the inflow Alfvénic Mach number and verify how the flow modifies the geometrical structure of the bow shock when the value of the plasma β is varied.

In Fig. 6.18 we show global views of the bow shock solutions for a fixed $M_{Ax} = 1.5$ and β varying from 0.1 to 0.9. It follows from Eq. 6.3 that the critical plasma β under which switch-on shocks can exist is $\beta = 0.7$. For plasma β values larger than the critical value of $\beta = 0.7$, the upstream flow is pressure-dominated and the bow shock has the traditional single-front topology that is also encountered in hydrodynamic bow shocks. When the plasma β drops below 0.7, however, the inflow becomes magnetically dominated. A concave-outward dimple forms in the leading shock front and a second shock front appears. This second shock front thus appears precisely when the plasma β becomes lower than the critical plasma β under which switch-on shocks are possible.

Fig. 6.19 shows a detailed representation of the flow near the stag-

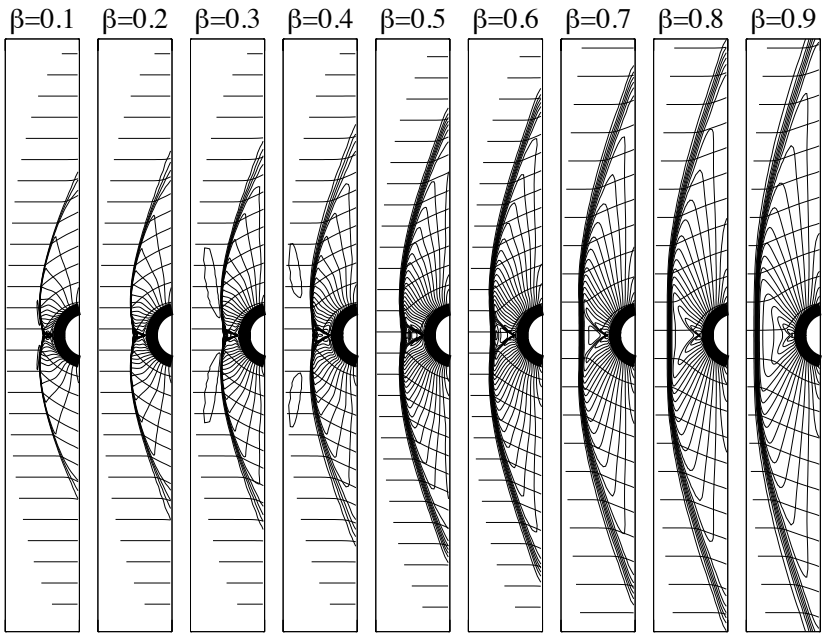

Figure 6.18: *Stationary bow shock solutions for fixed* $M_{Ax} = 1.5$ *and for varying plasma* β *(*80×80 *grids,* $x \in [-0.35, 0]$, $y \in [-1.4, 1.4]$*). Density contours pile up in shocks, and streamlines come in horizontally from the left. For plasma* β *values larger than the critical value of* $\beta = 0.7$ *the upstream flow is pressure-dominated, and the bow shock has the traditional single-front topology that is also encountered in hydrodynamic bow shocks. When the plasma* β *drops below* 0.7 *however, the upstream flow becomes magnetically dominated (switch-on shocks occur). A concave-outward dimple forms in the leading shock front and a second shock front appears.*

nation streamline for the bow shock solutions with varying plasma β of Fig. 6.18. We find again that the topology of Fig. 6.7 is universal for flows with plasma β values below the critical switch-on value ($\beta < 0.7$). The dimpling becomes more pronounced as the plasma β is decreased. For smaller plasma β values, the central interaction region in front of the cylinder becomes smaller. As a consequence, the shock E–G of Fig. 6.7 can not be identified for the flow with $\beta = 0.1$ with the resolution of Fig. 6.19. More detailed plots (not shown) do, however, show that shock E–G is present also for the flow with $\beta = 0.1$. For plasma

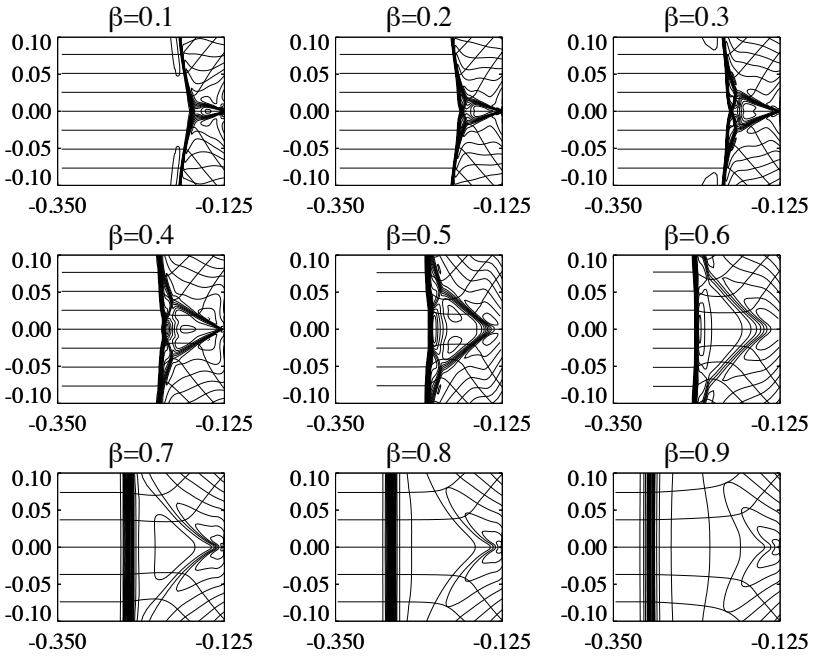

Figure 6.19: *Detailed representation of the flow near the stagnation streamline for the bow shock solutions with varying plasma β and for fixed $M_{Ax} = 1.5$ (80×80 grids). Density contours pile up in shocks, and streamlines come in horizontally from the left. Under the critical switch-on value for the plasma β, the leading shock front dimples and a second shock front appears. Additional discontinuities can be seen between the two shock fronts.*

$\beta = 0.7$, which is the critical value, the secondary (stationary) wave has only nearly steepened into a shock. Shock E–G can not be identified for this critical value of the parameters. For $\beta = 0.8$ the secondary waves are still present, but they have not steepened into shocks any more. The secondary waves are even weaker for $\beta = 0.9$, and the simple single-front bow shock topology of Fig. 6.6a is recovered. We can thus conclude that for all the flows with magnetically dominated upstream states ($\beta < 0.7$), the topology of Fig. 6.7 is recovered. The shapes, sizes and shock strengths of the shock parts present in the topology of Fig. 6.7, vary when β is varied in the switch-on regime. The dimple effect is more pronounced for smaller β.

As a remark, we can say that in the parameter regime under consideration, the stand-off distance of the bow shocks on the stagnation

line [114] does not seem to be influenced by changing M_{Ax} while keeping β constant (Fig. 6.17), whereas the stand-off distance increases for increasing β while M_{Ax} is kept constant (Fig. 6.19). This is consistent with observations of planetary bow shocks [114].

The main conclusion from the parameter study described in this Section is that there are two basic topologies for symmetrical 2D MHD bow shock flows. When the magnetic field is strong enough for the intrinsically magnetic effect of switch-on shocks to occur, we call the upstream flow magnetically dominated. When the magnetic field is too weak for switch-on shocks to occur, we call the upstream flow pressure-dominated. For pressure-dominated upstream flows a single-front topology is obtained which is the same as the well-known topology of hydrodynamic bow shock flows. We call this topology the pressure-dominated MHD bow shock topology, and we say that the MHD bow shock flow is pressure-dominated. For magnetically dominated upstream flows, we find the complex bow shock topology sketched in Fig. 6.7. We call this topology the magnetically dominated MHD bow shock topology, and we say that the MHD bow shock flow is magnetically dominated. The bifurcation between the two basic topologies occurs precisely on the border between the pressure-dominated and magnetically dominated parameter regimes as defined in terms of the occurrence of switch-on shocks. The complexity of the magnetically dominated MHD bow shock topology is due to intrinsically magnetic effects. The magnetically dominated MHD bow shock topology was previously unknown.

The existence of two basic MHD bow shock topologies proven in this Section is an *a posteriori* justification for the terminology of magnetically dominated versus pressure-dominated upstream states, bow shock flows and bow shock flow topologies which we have been using since the Introductory Chapter. In the next Chapter we show, although less extensively than for the 2D case, that the 3D flow of a superfast MHD plasma over a sphere also exhibits two basic bow shock topologies, with a clear bifurcation again arising precisely on the border between the pressure-dominated and magnetically dominated parameter regimes. The terminology we use to refer to these two basic bow shock flow topologies is thus universally valid for MHD bow shock flows in 2D and in 3D.

6.4 Characteristic analysis and steady compound shocks

In the present Section we further investigate the complicated magnetically dominated bow shock flow discussed in Sec. 6.2 using the characteristic properties of the steady MHD equations in two space dimensions (in the xy plane). The theory of MHD characteristics described

in Sec. 3.2 is used extensively. A geometric view of this steady flow is presented in terms of transition lines, cusping of characteristics, limiting lines, and elliptic and hyperbolic regions in the flow. This analysis yields a clear insight into a complicated nonlinear MHD flow with interacting shocks, and the consistency of the interpretation in terms of characteristics further validates the numerical results discussed above. In the recent literature, characteristic analysis of steady MHD flows has been applied to the study of astrophysical flows [62, 131, 163, 19] and stationary symmetric and transonic flows [93, 53]. In these papers analytical solutions of the steady MHD equations in two dimensions (2D) are obtained under various assumptions of self-similarity. The presence of shocks and the absence of any self-similarity assumption in the bow shock flows to be analyzed in this Section are new elements not treated in earlier characteristic analysis of MHD flows [62, 131, 163, 19, 93, 53].

In Sec. 6.2, the planar magnetically dominated bow shock solution was shown to contain an intermediate shock which is preceded and followed by steady rarefactions with the particular property that the normal plasma velocity is equal to a normal characteristic speed at the points where the rarefactions are attached to the shock (Fig. 6.15). This is one of the basic properties of an xt compound shock [90, 12] (see Sec. 3.3.5). However, the correspondence between xt compound shocks (with an attached simple wave rarefaction which is continuously expanding in time), and steady wave structures in two space dimensions (xy), is not immediately clear and does not follow trivially from the respective governing equations, although a general conceptual analogy can be expected between wave structures in the xt and the xy planes, such as demonstrated for compressible fluid dynamics [160]. Such a correspondence has also been worked out analytically for simple MHD waves in the xt and the xy planes [85]. In the present Section we explore the correspondence between complex wave patterns in the xt and the xy planes using characteristic properties of the steady MHD equations in two space dimensions (xy).

The characteristic analysis of the magnetically dominated multiple-front MHD bow shock flow is quite complicated, so it is useful to gain some insight from more simple configurations first. We start out with the simple case of a traditional hydrodynamic bow shock flow, followed by a discussion of the characteristic analysis of a pressure-dominated single-front planar MHD bow shock flow, before we proceed with the case of the magnetically dominated multiple-front planar MHD bow shock flow. We relate the results of the analysis of this flow to recent findings on stationary symmetric flows [53] and on xt MHD compound shocks [12, 110].

6.4.1 Hydrodynamic bow shock

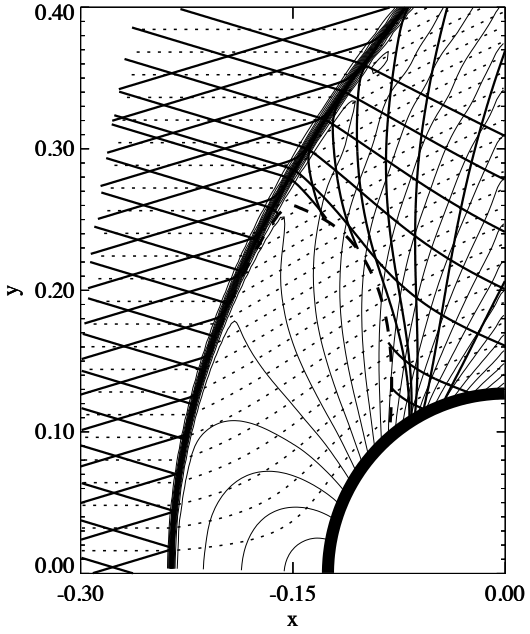

Figure 6.20: *Bow shock flow for the hydrodynamic case ($v_x = 2$, $B_x = 0$).*

Fig. 6.20 shows the simulation result of a hydrodynamic bow shock with $v_x = 2$ and $B_x = 0$ for the incoming flow. We take $\rho = 1$ and $p = 0.2$ for the inflow of all the bow shock flows presented in Sec. 6.4. The shock is clearly seen where the density contours (thin solid lines) are piling up. The streamlines (dotted) are double characteristics, and s and h_s are the corresponding Riemann Invariants along these characteristics. The thick solid lines are the two families of hydrodynamic characteristics (Mach lines [20]) making equal angles ψ with the streamlines. The thick dashed transition line is the $M = 1$ contour, separating the subsonic elliptic region close to the cylinder from the rest of the flow, which is supersonic and thus hyperbolic. The Mach lines are perpendicular to the streamlines at the transition line, corresponding to case (b) of Fig. 3.5.

Limiting characteristics [20, 53] (or limiting lines) are the convex hulls of characteristics which appear when characteristics of one family start to pile up and develop those convex hulls. Limiting characteristics can not exist in real flows, unless they are perpendicular to the streamlines. They are generally avoided through the appearance of shocks [20, 53], because at the location of the limiting characteristic the solution would be multi-valued. In the bow shock flow of Fig. 6.20 it is indeed seen that limiting lines are not present, but that shocks bring the flow from the upstream supersonic state to a downstream elliptic (close to the stagnation point) or hyperbolic (further away from the stagnation point) state [53].

6.4.2 Pressure-dominated MHD bow shock

In Fig. 3.6 we have shown the simulation result of a pressure-dominated fast MHD bow shock with $v_x = 2$ and $B_x = 1$ for the incoming flow. The inflow plasma β is low, but these inflow parameters do not allow for switch-on shocks, so that we get a simple traditional single-front MHD bow shock. The characteristic structure of this flow, which was discussed in Sec. 3.2, is very similar to the structure of the hydrodynamic flow. The angle ψ is a little larger, such that the bow shock and the characteristics are opened up a little compared to the hydrodynamic case. The influence of the magnetic field on this angle is clear: the angle is always larger than the corresponding hydrodynamic angle ($B_x = 0$), as

$$\sin^2 \psi_{MHD} = \frac{M^2 + M_A^2 - 1}{M^2 M_A^2} \geq \sin^2 \psi_{HD} = \frac{1}{M^2} \tag{6.4}$$

for supersonic flow ($M^2 \geq 1$). The comments regarding limiting characteristics that were given in the hydrodynamic case, also apply to this fast MHD bow shock flow.

6.4.3 Magnetically dominated MHD bow shock

Fig. 6.21 shows the simulation result of a magnetically dominated MHD bow shock flow with $v_x = 1.5$ and $B_x = 1$ for the incoming flow. This is the flow discussed in Sec. 6.2. The angle ψ in the upstream part is larger than in the single-front case of Sec. 6.4.2. The bow shock is opened up even more and a 'dimple' appears in the shock front near the stagnation streamline, where the front is now curved convex outward from the cylinder. A second shock front is seen to have separated from the leading shock front. Additional discontinuities can be seen between these two shock fronts.

These complex shock interaction phenomena lead to a flow which is quite a bit more complicated in terms of characteristic analysis. The dotted lines again indicate the streamlines, and the thick solid lines

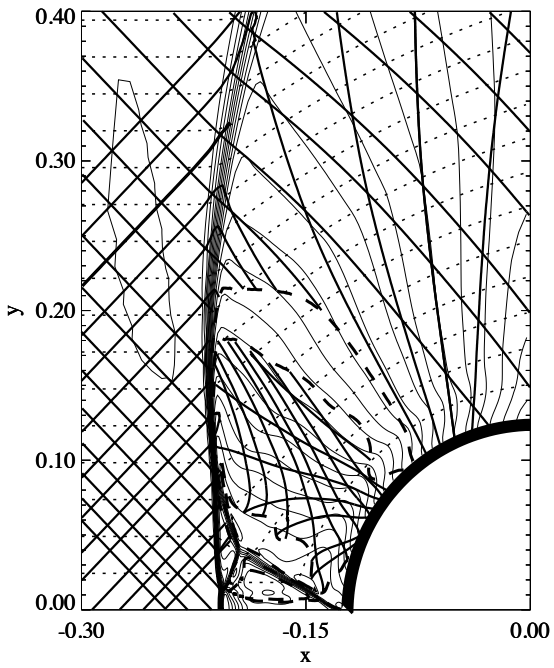

Figure 6.21: *Magnetically dominated MHD bow shock flow ($v_x = 1.5$, $B_x = 1$). Density contours (thin solid lines) pile up in the shocks. The streamlines (which are also magnetic field lines) are dotted. The thick solid lines are two families of fast characteristics making equal angles with the streamlines. Several elliptic and hyperbolic regions are present.*

indicate the two families of characteristics which are of the slow or fast type depending on the location in the flow. Several separate elliptic regions can be seen.

Fig. 6.22 presents an analysis of the hyperbolicity of the flow. The thick solid line is the $\beta^* = 1$ contour. The $M = 1$ contour (thick dashed), the $M_A = 1$ contour (thick dotted), and the $M_{cusp} = 1$ contour (thick dash-dotted), are the transition lines between elliptic an hyperbolic regions. We can label the regions according to the classification of Fig. 3.4. The incoming flow is hyperbolic of the type Hf2. Downstream of

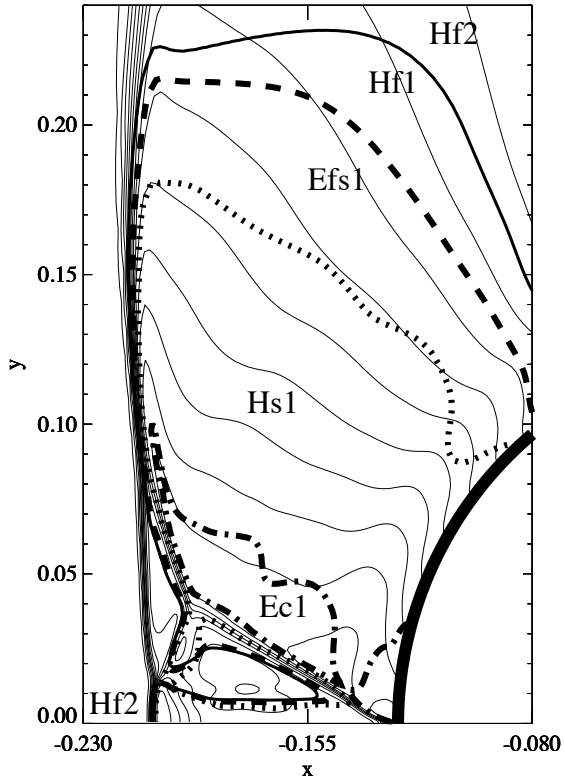

Figure 6.22: *Elliptic and hyperbolic regions in the bow shock flow. Density contours (thin solid lines) pile up in the shocks. The* $\beta^* = 1$ *contour (thick solid), the* $M = 1$ *contour (thick dashed), the* $M_A = 1$ *contour (thick dotted), and the* $M_{cusp} = 1$ *contour (thick dash-dotted) separate the different regions.*

the leading and the second shock fronts, and starting from above, the flow is first hyperbolic of the type Hf2, and becoming hyperbolic of the type Hf1 as the $\beta^* = 1$ contour is crossed. Crossing the $M = 1$ contour brings us into an elliptic region of type Efs1, followed by a hyperbolic region of type Hs1 when the $M_A = 1$ contour is crossed. In Fig. 6.21

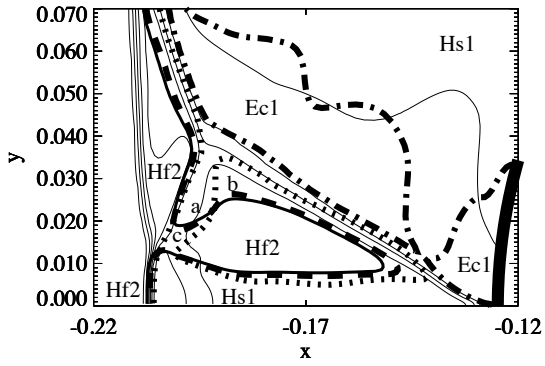

Figure 6.23: *Elliptic and hyperbolic regions in the bow shock flow near the stagnation streamline. Density contours (thin solid lines) pile up in the shocks. The $\beta^* = 1$ contour (thick solid), the $M = 1$ contour (thick dashed), the $M_A = 1$ contour (thick dotted), and the $M_{cusp} = 1$ contour (thick dash-dotted) separate the different regions. Region a is Hs1, region b is Efs1, and region c is Efs2.*

we see that the characteristics are perpendicular to the streamlines at these transition lines. Further down, we reach the elliptic region of type Ec1 as the $M_{cusp} = 1$ contour is crossed. At this transition line, the characteristics show the expected cusping behavior of Fig. 3.5c, as can be seen in Fig. 6.21.

In Fig. 6.23 we show a more detailed plot of the interaction region near the stagnation streamline. The incoming flow is Hf2, and it remains Hf2 through the fast shock DE. Shock EG brings the flow into a Hs1 region (region a), as we cross the $\beta^* = 1$, $M = 1$, and $M_A = 1$ contours simultaneously. From region a, crossing the $M_A = 1$ contour leads us to a Efs1 region (region b), and crossing the $\beta^* = 1$ and $M = 1$ contours leads to a Efs2 region (region c). Near the stagnation streamline at the bottom, shock EF brings the flow into a Hs1 region, as the $\beta^* = 1$, $M = 1$, and $M_A = 1$ contours are crossed simultaneously. Enclosed between regions c, b, and the Hs1 region at the bottom, we find a Hf2 region.

As could be expected, we do not encounter limiting lines in this flow, but instead we find shocks. Shock transitions exist between two hyperbolic regions (for example, from Hf2 to Hf2 through shock DE, and from Hf2 to Hs1 through shocks EG, EF, and BD), between a hyperbolic and an elliptic region (for example, from Hf2 to Efs1 above point B ($M_A = 1$

downstream of point B), and from Hf2 to Ec1 through shock DG), and apparently also between elliptic regions of different types (from region b (Efs1) to Ec1 through shock GH), although we have to remain careful with our conclusions as the numerical resolution is not very high in this small region. This last type of shock transition from elliptic to elliptic may be surprising at first sight, but a similar theoretical result has recently been reported, based on explicit solutions for stationary symmetric self-similar MHD flows, stating that this type of shock transition is possible [53]. We can conclude that the flow configuration, characteristic analysis, and types of shock transitions of our interacting bow shock solution are illustrations and 2D extensions of many of the recent theoretical results obtained from analysis of stationary symmetric self-similar MHD flows [53].

We now investigate if we can identify steady compound shocks in the complex bow shock flow. A steady compound shock should have the following properties, based on carrying over the geometry of characteristics from the xt case to the xy case. First, the flow should be hyperbolic on the two sides of the shock. Second, the shock should have a rarefaction attached to it which is a simple wave with one family of characteristics consisting of straight lines. Third, the xy characteristics should be parallel to the shock in the xy plane, such that the flow is sonic in the xy plane where the shock is attached to the rarefaction. We now analyze several wave structures in the simulated bow shock flow to see if they fulfill these criteria.

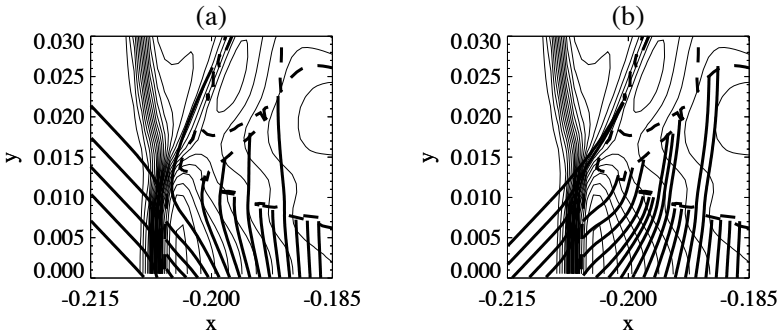

Figure 6.24: *Two families of characteristics (thick solid) near the shock EF. The thin lines are density contours. The characteristics enter the shock, so this is not a compound shock.*

We start with the leading shock at the stagnation streamline. Fig. 6.11a suggests that this could be a steady compound shock. Fig. 6.23

confirms that the flow is hyperbolic on both sides of the shock, but the behavior of the two characteristic families in Fig. 6.24 shows that this is not a steady compound shock as we have defined above. Neither of the characteristics is parallel to the shock where the rarefaction is attached to the shock, and the two families are not straight but interact in the rarefaction which is thus not a simple wave. This conclusion is consistent with the discussion in Sec. 6.2, where it was shown that this rarefaction is of a different physical origin, being a 2D effect associated with the converging flow behind the shock. The plasma speed equals neither of the wave speeds where the rarefactions are attached to the shock, as was shown in Fig. 6.11f–h.

Fig. 6.24 also reveals another interesting phenomenon. As the pressure in the rarefaction in Fig. 6.11b drops when going to the right, the characteristics in 6.24 straighten and form one coinciding limiting characteristic where the pressure reaches a constant state after the rarefaction (at approximately $x = -0.185$). This limiting characteristic is allowed because the streamlines are perpendicular to it. This limiting line is a locus of weak discontinuity, where the pressure is continuous, but the slope of the pressure has a discontinuity. This weak discontinuity connects the rarefaction region with the uniform flow region behind it, and Fig. 6.11h shows that the flow is indeed sonic at the location of this weak discontinuity. The rarefaction region bordering the uniform region is, however, not a simple wave region, such that this special configuration with a limiting characteristic seems to be an exception to the rule that a uniform region in a stationary 2D flow can only be bordered by a simple wave region [20].

We now turn our attention to intermediate shock EG. Fig. 6.15 suggests that this could be a steady compound shock with an embedded 1=2—3=4 intermediate shock. The behavior of the two characteristic families shown in Fig. 6.25, shows that the flow is hyperbolic on both sides of the shock. The second family of characteristics (Fig. 6.25b) is parallel to the shock on the right, and goes into the shock on the left. The characteristics of this family are straight on the right of the shock, indicating a simple centered slow rarefaction wave with the characteristics apparently converging in point G. The first family of characteristics (Fig. 6.25a) is parallel to the shock on the left, and goes into the shock on the right. The characteristics of this family are straight on the left of the shock. The intermediate shock is thus preceded and followed by simple rarefaction waves which are sonic at the point where they are attached to the shock. This rarefaction-shock-rarefaction structure has thus all the defining properties of a compound shock. This compound shock is sonic on the two sides, so we can call this newly identified steady wave structure a *double steady compound shock* (Fig. 6.26b). The analogous xt structure has been predicted theoretically recently in the context of xt

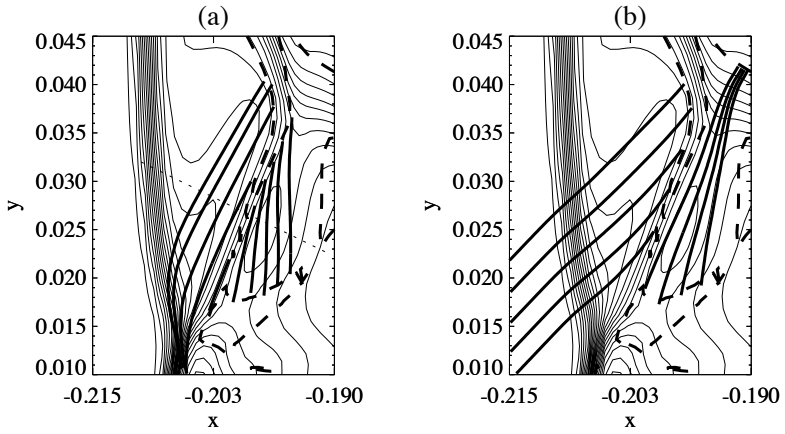

Figure 6.25: *Two families of characteristics (thick solid) near the intermediate shock EG. The thin lines are density contours. On each side of the shock, the characteristics of one family are straight lines and become parallel to the shock, so this is a double compound shock.*

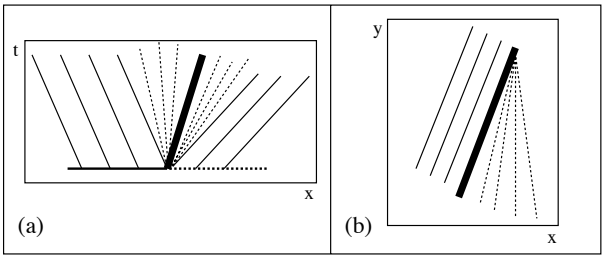

Figure 6.26: *(a) Sketch of the recently theoretically predicted double xt compound shock. The shock (thick) is preceded and followed by rarefactions (thin dotted), which are attached to the shock with characteristics parallel to the shock. (b) Sketch of the topology of the characteristics near the double xy compound shock which is present in our simulation results. The shock (thick) is preceded and followed by simple wave rarefaction regions, which are attached to the shock with straight characteristics parallel to the shock.*

compound shocks [110] (Fig. 6.26a). It has not been identified yet in xt simulations, but it is noteworthy that we encounter the analogous steady xy structure in our 2D simulation results. This new steady structure is a

manifestation of the non-convex nature of the MHD equations, just like the sonic intermediate shocks embedded in xt time-dependent compound shocks are a manifestation of this property. We have thus established by explicit example a remarkably complete analogy between the characteristic structure of time-dependent compound waves in the xt plane and the characteristic structure of steady compound waves in the xy plane. Following Myong and Roe [110], we argue that this steady compound shock occurs as a substitute for a 2—3 intermediate shock which is undercompressive and inadmissible in the planar case (see Chap. 9).

We suggest the following physical relationship between the two kinds of compound shocks, those of time-dependent flows in the xt plane and those of steady flows in the xy plane. If an initial plane compound shock taken in the time-dependent sense and moving in xyt space with a sonic fast rarefaction (which is expanding in time) attached to it, were to slow down and become steady, then such a structure could conceivably retain the property that the now steady rarefaction is sonic ($v_\perp = c_{f\perp}$) at the point where it is attached to the shock. This is precisely the defining property of a fast characteristic in steady xy space (see Sec. 3.2), which means that all the points at the locus where the rarefaction is attached to the shock with a sonic speed, lie on a steady xy characteristic parallel to the shock, thus explaining that the steady xy characteristic is parallel to the shock where the rarefaction is attached to it. This observation clarifies a natural relationship between xt and xy compound shocks, which could possibly be further explored by explicit numerical simulation of the above proposed scenario. It also explains why the flow in terms of xt wave speeds is sonic where the rarefactions are attached to the shocks in steady compound shocks, as can be seen in Fig. 6.15bc.

6.5 Symmetry and stability

In this Section we investigate the global stability against perturbations of the symmetrical magnetically dominated bow shock solutions discussed in the previous sections.

All the simulation results shown in this Chapter up till now were calculated on a grid restricted to the upper left quadrant with the top-bottom symmetry explicitly imposed. As mentioned before, this flow in the upper quadrant can be interpreted physically as the flow over a perfectly conducting plate with a semi-circular bump or corner. The numerical results seemed to indicate that the obtained flow topology is stable against perturbations, and in this Section we give some more elements to support this.

The full problem of a flow around a cylinder should in theory have the same symmetrical solution, because the initial condition and the

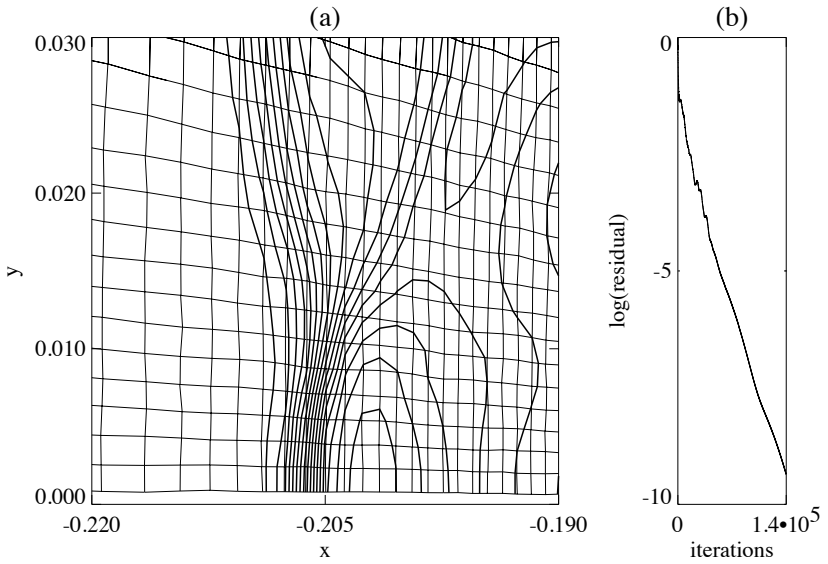

Figure 6.27: *LF flow solution and convergence for the symmetrical bow shock problem on a randomly perturbed grid* (80×80). *The grid shown in (a) is a grid of cell centers.*

boundary conditions are symmetrical, and the MHD equations should conserve this symmetry. However, the stationary solution and its topology may be globally unstable against non-symmetrical perturbations. Such an instability might be triggered by explicit non-symmetrical perturbations, but also by non-symmetrical grids or a numerical code which is not perfectly symmetrical.

Fig. 6.27 shows that we obtain the complex bow shock topology for a flow restricted to the upper quadrant when we perturb the corner points of the finite volume cells in a random way, and that the solution converges to a perfect steady state. The corner points which lie on the boundary of the simulation domain were not perturbed. Fig. 6.28, however, shows that the full problem of the magnetically dominated flow around a cylinder in the switch-on regime without imposed symmetry leads to a very a-symmetrical unsteady flow when the grid is randomly perturbed. This is an indication that the symmetrical solution is unstable against non-symmetrical perturbations, although it is not a proof.

Another indication is given by the following observations. We consider the flow around a cylinder and also simulate the flow behind the cylinder. Fig. 6.29 shows the bow shock flows for inflow parameters

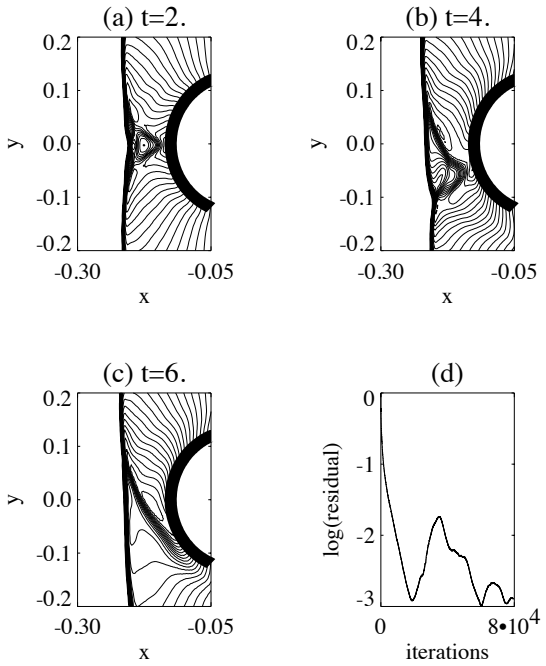

Figure 6.28: *LF flow solution (120 × 240 grid) and convergence for the magnetically dominated bow shock problem on a randomly perturbed full grid without explicitly imposed symmetry.*

$\rho = 1$, $p = 0.2$ and $v_x = 1.5$, simulated on the whole domain. The flow in the wake of the cylinder is subfast, so we use the characteristic boundary conditions described in Sec. 4.2.6 for the outer boundary. Fig. 6.29a shows the hydrodynamic case ($B_x = 0$), and Fig. 6.29b shows the case of a pressure-dominated MHD bow shock ($B_x = 0.5$). The two flows show the traditional pressure-dominated concave-inward bow shock shape and topology. We have investigated the stability of these flows against non-symmetrical perturbations by adding a small uniform upward or downward vertical velocity $v_y = \pm 0.01$ to the initial condition or by restarting the simulation from the stationary solutions of Fig. 6.30 perturbed by such a vertical velocity. In all these cases the flow returned to the stationary solutions of Fig. 6.29, which indicates that these traditional bow shock topologies are stable against non-symmetrical perturbations.

Fig. 6.30 shows the bow shock flows for magnetically dominated inflow parameters $\rho = 1$, $p = 0.2$, $v_x = 1.5$ and $B_x = 1$, such that

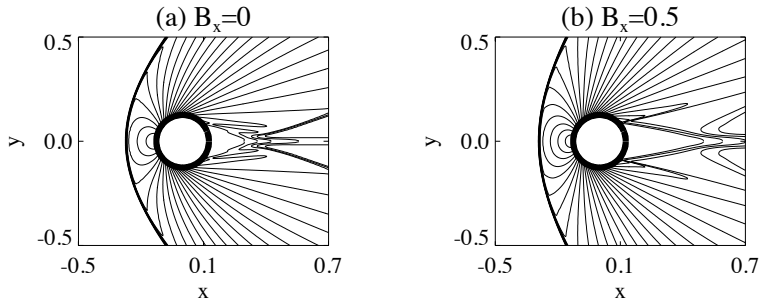

Figure 6.29: *Bow shock flows around a cylinder. (a) Hydrodynamic flow:* $M_x = 2.6$ *and* $B_x = 0$. *(b) Pressure-dominated MHD flow:* $M_x = 2.6$, $M_{Ax} = 3$ *and* $B_x = 0.5$

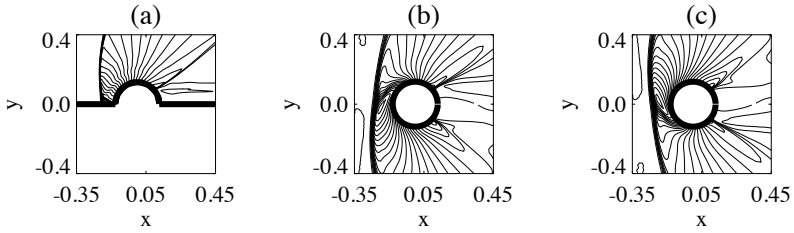

Figure 6.30: *Magnetically dominated MHD bow shock flow. (a) Symmetrical solution on a domain restricted to the upper half plane. (b) Non-symmetrical solution obtained when starting from an initial condition perturbed with a small downward velocity. (c) Non-symmetrical solution obtained when starting from an initial condition perturbed with a small upward velocity.*

$M_{Ax} = 1.5$. Fig. 6.30a shows the flow simulated in the upper half plane (400×400 grid), with the symmetry on the stagnation line explicitly imposed. In front of the cylinder we obtain the same stationary magnetically dominated flow topology that was described earlier. Simulation after perturbation of the initial condition or the stationary flow as described above, leads invariably back to the same stationary solution of Fig. 6.30a. Figs. 6.30b and c, however, show a completely different behavior for simulations on the full domain (100×200 grids). Perturbation of the initial condition with a small uniform upward (c) or downward (b) vertical velocity $v_y = \pm 0.01$, results in a flow topology which is *entirely*

different from the symmetrical result. This is a strong indication that the symmetrical solution is unstable against non-symmetrical perturbations. The resulting non-symmetrical flow is intermittent. The leading shock front is again dimpled, and the leading shock front is followed by a secondary shock front. The V-shaped secondary feature of Fig. 6.2 is, however, completely absent in this non-symmetrical flow result.

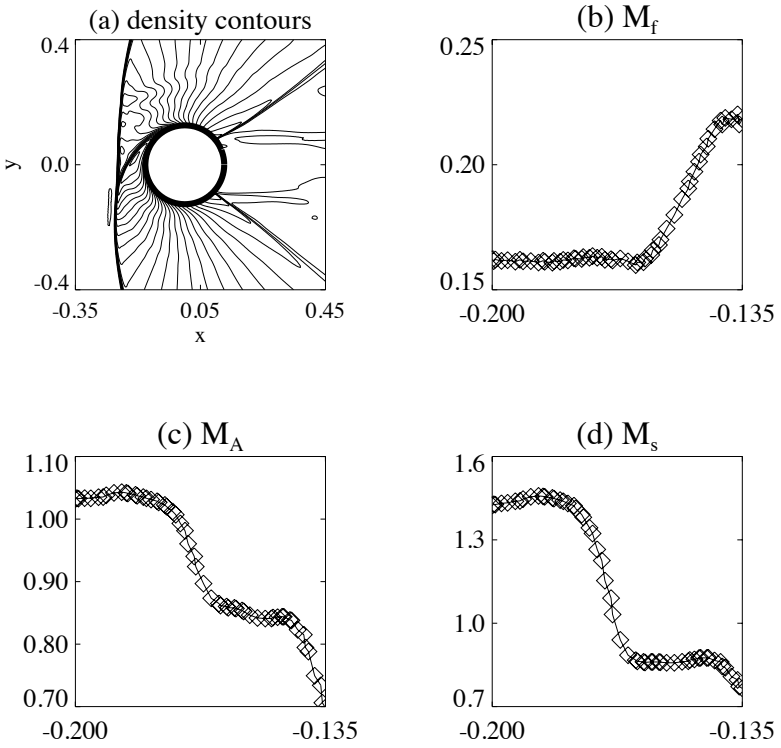

Figure 6.31: *(a) Non-symmetrical magnetically dominated bow shock flow. (c–d) Cuts along a line perpendicular to the secondary shock front.*

In Fig. 6.31 we determine the MHD shock type of the secondary shock front for a simulation on a 400×800 grid. Figs. 6.31c–d show cuts along a line perpendicular to this secondary shock. This shows that the shock is an intermediate shock of the 2–4 type, close to a 2=3–4 slow switch-off shock. This shock is thus of the same type as shock D–G–H–I in the topology of the symmetrical solution sketched in Fig. 6.7. In the next

Chapter we break the symmetry by introducing a small angle between the magnetic field and the velocity for the flow over a sphere. We obtain solutions which are topologically similar to the solutions of Figs. 6.28, 6.30 and 6.31.

We have to admit that in most cases we did not obtain the symmetrical solution when we performed our simulations of the non-perturbed problem on the full grid (the left half plane or the full plane) without the symmetry explicitly imposed at the stagnation line. This is because our code and the grid used are not perfectly symmetrical. It is extremely difficult to make a numerical code perfectly symmetrical, and the best way to make sure that simulation results are symmetrical, is to impose the symmetry explicitly, as we have done for our simulations on the restricted domain of the upper left quadrant.

What does this conclusion on instability imply for the symmetrical magnetically dominated bow shock topology presented and discussed in the previous Sections? The symmetrical solution is likely to be a *meta-stable* solution in the case of the full flow around a cylinder. Meta-stable solutions are not necessarily unphysical and can arise in physical systems under special conditions — the reader may recall the case of an undercooled fluid for instance —, but it is not likely to find the topology of Fig. 6.7 with a V-shaped secondary front in real stationary bow shock flows around obstacles, because small perturbations are probably sufficient to change this topology into the topology of Fig. 6.31a.

The symmetrical solution and the detailed discussion remain relevant for several reasons, however. First, we have shown that the symmetrical solution obtained by simulation in the upper left quadrant with the symmetry explicitly imposed is stable against perturbations as long as the symmetry remains strongly imposed. This flow thus constitutes an example of a stable 2D MHD flow in which various types of intermediate and compound shocks are present, and this rich structure and topology makes this flow certainly interesting in its own right. The physical interpretation as a flow over a perfectly conducting plate with a semi-circular bump or corner does not immediately seem to have realistic applications, but our solutions are excellent explicit examples to illustrate similar topologies and transitions between hyperbolic and elliptic regions involving shocks that may possibly be found in related configurations with astrophysical relevance. Second, the non-symmetrical topology of Figs. 6.30b and c still is typified by two conspicuous morphological properties, namely a concave-outward dimple in the leading shock front and a secondary shock front following the leading front. These important newly discovered properties remain intact from the symmetrical solution. Moreover, in the next Chapter we show that the V-shaped structure from the symmetrical topology can still arise in non-symmetrical configurations as a time-dependent *transient* structure (as in Fig. 6.28).

The detailed study performed in Secs. 6.2 and 6.4 of the shock types and waves present in the symmetrical solution turns out to be very helpful in the analysis of these time-dependent flows for the non-symmetrical case.

The reader may wonder why we do not study the stability of the symmetrical solution by perturbing the *boundary conditions* together with the initial condition. Indeed, it seems natural to introduce a-symmetry by introducing a small angle between the velocity and magnetic field in the boundary conditions of the stationary problem. In a 2D flow, however, we cannot do this because for a stationary solution in 2D the flow necessarily has to be field-aligned when ideal walls are present in the problem. Equivalently, and more physically, we can say that the magnetic flux would pile up in front of the cylinder in the case of non-field-aligned 2D flow, because field lines cannot break in ideal MHD. The non-field-aligned 2D ideal MHD problem would thus not lead to a steady state, since the field lines cannot be advected across the cylinder. In the case of field-aligned flow, the magnetic flux is split into two equal parts which can flow around the cylinder on the left and the right sides. In the case of 3D flow over a perfectly conducting sphere, however, we can introduce an angle between the velocity and magnetic fields. A non-symmetrical stationary flow then results, because the field lines can slip over the top and the bottom of the sphere in 3D space. This is studied in the next Chapter. There we also perform a simulation for the special case of field-aligned flow over a sphere, and we obtain a symmetrical flow configuration with a topology similar to the topology sketched in Fig. 6.7. We can study the stability of this symmetrical solution by introducing a small angle between the fields. In fact this way to study the stability of the symmetrical flow is more rigorous and well-defined than the approach to stability study of the 2D flow given in this Section.

6.6 Conclusion

Let us summarize the physical lessons we have learned in this Chapter. There are two basic topologies for symmetrical 2D MHD bow shock flows. For pressure-dominated upstream flows a single-front topology is obtained which is the same as the well-known topology of hydrodynamic bow shock flows. For magnetically dominated upstream flows, the intrinsically magnetic phenomena of switch-on shocks and intermediate shocks cause the bow shock flow to assume a complex topology which was previously unknown. This magnetically dominated flow topology involves not only shock fronts composed of segments of different MHD shock types, but also a multitude of interacting fronts. The manner in which these shock types arise on a front or the presence of multiple fronts all relate to the dynamics of information transfer by the MHD charac-

teristic waves to guide the superfast flow around the obstacle. Put in these general terms, the numerical work presented in this Chapter has broadened our physical thinking on bow shock flows in MHD, in particular, and on hyperbolic systems with multiple characteristic waves, in general.